IV Escola de Primavera de Transição e Turbulência
Universidade Federal do Rio Grande do Sul
Pontifícia Universidade Católica do Rio Grande do Sul
Porto Alegre, RS, 27 de setembro a 1º de outubro de 2004

VORTICITY SHEDDING, ACOUSTIC RESONANCE AND TURBULENCE EXCITATIONS IN TUBE BUNDLES

Samir Ziada
McMaster University
Hamilton, Ontario, L8S 4L7
Canada
ziadas@mcmaster.ca

This paper focuses on the phenomenon of vorticity shedding in tube bundles and its relation to the acoustic resonance mechanism and the dynamic fluid forces exerted on the tubes. These phenomena are investigated by means of velocity, pressure and force measurements, as well as with the aid of extensive visualization of the unsteady flow structure at the presence and absence of acoustic resonance. Vorticity shedding excitation is shown to be generated by either jet, wake, or shear layer instabilities. The tube layout pattern (in-line or staggered), the spacing ratio, and Reynolds number determine which instability mechanism will prevail, and thereby the relevant Strouhal number for design against vorticity shedding excitation. Strouhal number design charts for vortex shedding in tube bundles are presented for a wide range of tube patterns and spacing ratios. With respect to the acoustic resonance mechanism, it is shown that the natural vorticity shedding, which prevails before the onset of resonance, is not always the source exciting acoustic resonance. This is especially the case for in-line tube bundles. This finding leads to the conclusion that separate "acoustic" Strouhal number charts must be developed to improve our ability to avoid acoustic resonances in new designs. To this end, the most recently developed charts of acoustic Strouhal numbers are provided. Finally, design charts of dynamic lift coefficients and bound spectra of turbulent fluid forces acting on the tubes are also presented.

Key words: Tube bundles, vorticity shedding, acoustic resonance, turbulant buffeting, flow excitations in tube bundles

1. Introduction

Flow-induced vibrations of heat exchanger tube bundles often cause serious damages resulting in lost revenue and high repair costs. A wide range of flow-induced vibration and noise problems in heat exchangers is reviewed by Païdoussis (1982). The excitation mechanisms causing flow-induced vibrations of tube bundles in cross-flows are generally classified as (a) tube resonance by vorticity shedding, (b) acoustic resonance, (c) turbulent buffeting and (d) fluid-elastic instability. This study focuses on the first three of these excitation mechanisms for the most common layout patterns of tube bundles. Figure (1.1) shows these patterns, classified into in-line (IL), parallel triangle (PT), normal triangle (NT), and rotated square (RS) arrays. Note that the normal square (NS) geometry is a special case of the general in-line pattern. As illustrated in Fig. (1.1), the parallel triangle array has staggered tubes, similar to NT and RS arrays. However, in contrast to the latter arrays, it allows the flow to proceed relatively freely along the lanes between adjacent tube columns, which is similar to the case of in-line tube pattern. For this reason, as will be shown in this paper, the flow excitations in IL and PT tube bundles display some common features, which are different from those observed in NT and RS arrays.

1.1. Excitation Mechanisms

A typical vibration response of a tube in a bundle showing the main features of the excitation mechanisms is given in Fig. (1.2). In the following, the main features of each mechanism are briefly introduced.

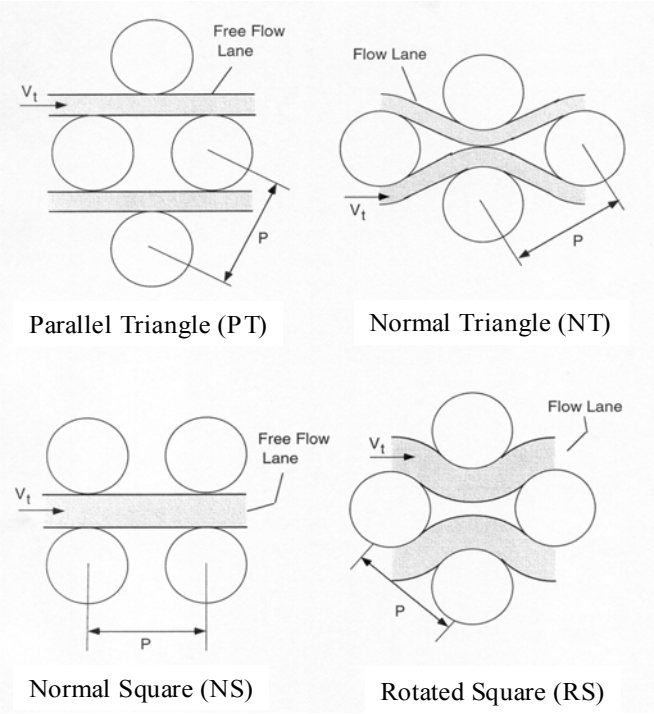

Figure 1.1. Standard layout patterns of tube arrays and corresponding patterns of flow "lanes" for a selected pitch ratio (P/d = 1.4).

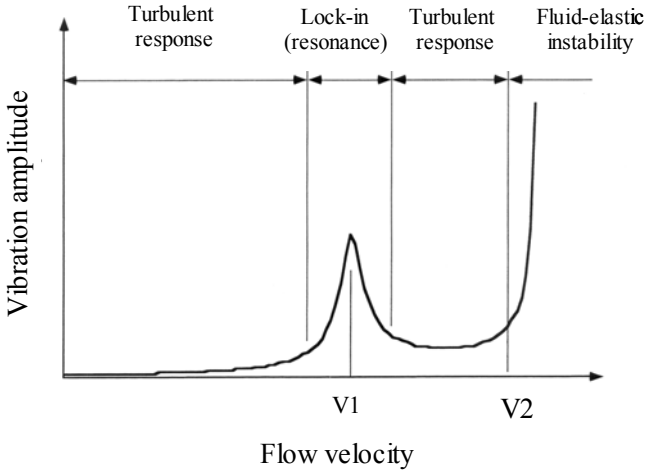

Figure 1.2. Typical vibration response of a tube in a bundle showing the characteristics of different excitation mechanisms. V1: critical velocity for tube or acoustic resonance; V2: critical velocity for fluid-elastic instability.

1.1.1. Vorticity shedding

Tube arrays in cross flow are excited, to varying degrees by periodic fluid forces, the frequency of which varies linearly with the flow velocity. This periodic excitation is variously known as: flow periodicity, Strouhal periodicity, or vorticity shedding. It appears in the turbulence and pressure spectra as a narrow band peak, which indicates that it is basically a periodic phenomenon. The turbulence spectra given in Fig. (1.3) illustrate the dependence of the vorticity shedding peak (f_v) on

the gap velocity (V_t). When the frequency of this vorticity shedding coincides with a mechanical resonance frequency of the tubes, resonant vibration and rapid tube damage can occur, especially in liquid flows. The flow velocity at which this occurs is known as the critical flow velocity for tube resonance, and the velocity range over which the tubes exhibit large amplitude vibration is referred to as the "Lock-in" range. The resonant response of a tube within the lock-in range is exemplified in Fig. 1.2. Although this type of excitation has been recognised since the 1950's, its cause has been disputed in the literature (Owen, 1965). However, recent studies have shown clearly that it results from periodic vortex formation in the space between the tubes (Weaver, 1993; Ziada et al., 1989; Ziada & Oengoeren, 1992).

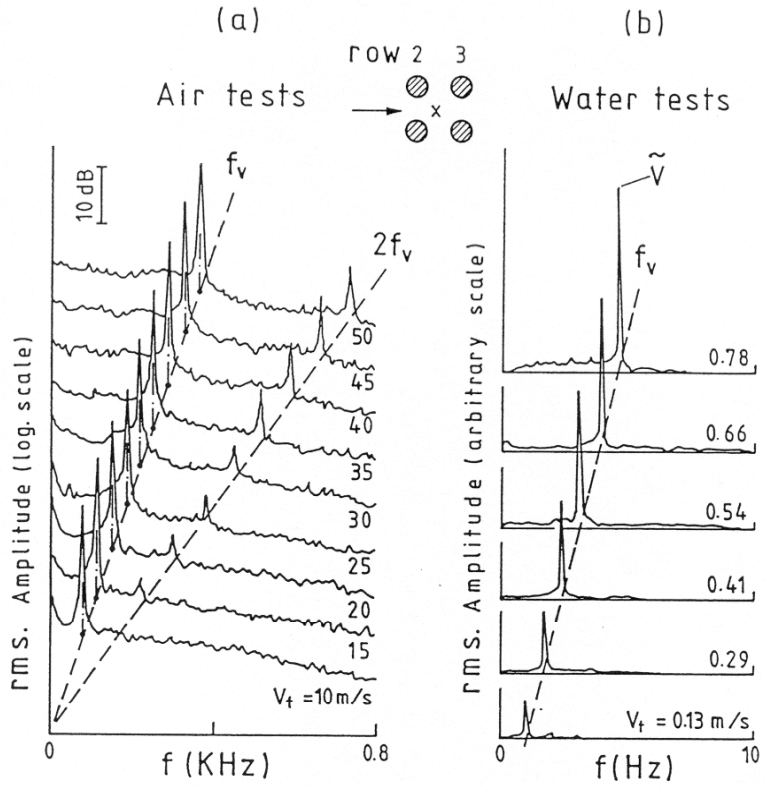

Figure 1.3. Typical spectra of fluctuating velocity behind the third row of an in-line tube bundle illustrating the nature of vorticity shedding. (a) air tests; (b) water tests; V_t: gap flow velocity; f_v: vortex shedding frequency.

1.1.2. Acoustic resonance

Acoustic modes of the tube bundle containers can also be excited by gas flow across the tubes. The excited modes are those consisting of acoustic standing waves in a direction normal to the tube axes and the flow direction, see Fig. (1.4). At resonance, an intense pure tone noise, which can reach 175 dB, is produced. This level is sufficiently high to disturb the operation of power plants and cause structural failure. The excitation mechanism of these resonances is strongly dependent on the tube layout pattern and spacing ratio.

1.1.3. Turbulent buffeting

Every tube bundle in cross flow is subjected to a broad band excitation due to the turbulence existing in the approach flow and that generated by the tubes of the bundle. Although the response of the tubes to turbulence excitation is generally small and does not cause short-term damage, it is the principal source of long term fretting wear at the tube supports. The rate of fretting wear, and therefore the lifetime of the equipment, depends on the amplitude of the turbulent response. Thus, in order to be able to estimate the life span of heat exchange equipment, which is especially

important for nuclear power generation, one needs an expression of the turbulent fluid forces acting on the tubes.

1.1.4. Fluid-elastic instability

This excitation mechanism is initiated due to the coupling between the tube motion and the fluid forces. A small extraneous displacement of the tube, due to turbulence for example, alters the flow pattern, resulting in a change in the fluid forces, which leads to further displacement. The change in the fluid forces may be displacement dependent, causing stiffness-controlled instability, or vibration velocity dependent, causing negative damping instability. In either case, when the flow velocity exceeds a critical value, the vibration amplitude grows very rapidly as illustrated in Fig. (1.2). Fluid-elastic instability is distinguished from the other mechanisms in that the destabilizing fluid forces disappear in the absence of the tube motion. Moreover, tube and acoustic resonance vibrations occur over a certain range of flow velocity, whereas tube instabilities are triggered abruptly when the flow velocity exceeds a critical value. This instability mechanism is outside the scope of this paper and interested readers are referred to the review paper by Price (1993).

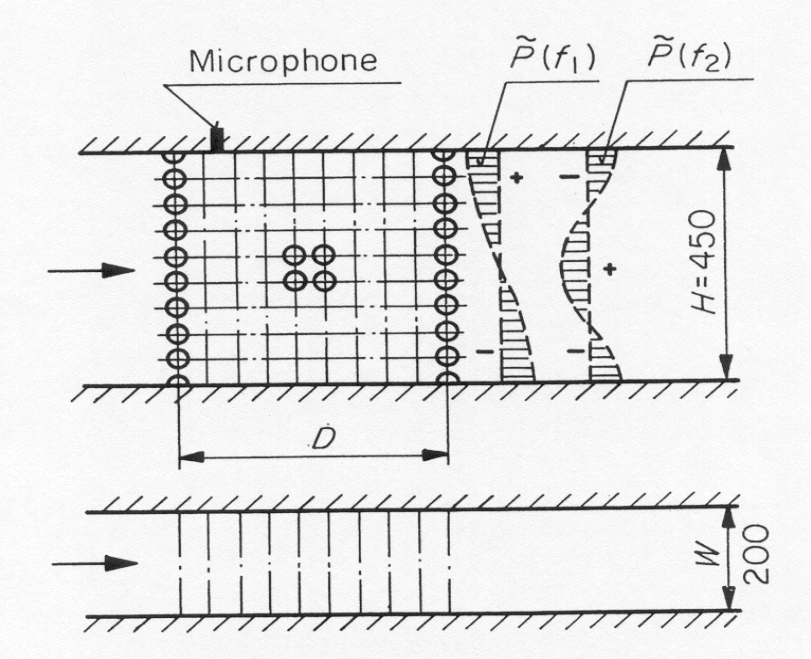

Figure 1.4. Schematic presentation of the wind tunnel test section illustrating the distributions of acoustic pressure associated with the first and second acoustic modes. $P(f_1)$: pressure distribution of first acoustic mode; $P(f_2)$: second mode.

1.2. Brief Outlines of Contents

Investigation of the vorticity shedding excitation in tube bundles and its relation to acoustic resonance excitation and generation of dynamic fluid forces in the tubes requires a spectrum of experimental techniques to measure fluctuating flow velocity between the tubes, pressure fluctuations on the surface of the tubes, dynamic fluid forces acting on the tubes, and sound pressure on the test section wall. Additionally, flow visualization of unsteady flow structures at different locations within the bundles and the phase of these flow activities is essential to reveal the global feature of flow instability and its dependence the tube layout patter and spacing ration. The experimental techniques used to investigate these phenomena are described briefly in the next section. For further details the reader is referred to Ziada & Oengoeren (1992, 1993, 2000) and Oengören & Ziada (1992a, 1992b, 1998).

The normal triangle array pattern will first be discussed. Attention will then be focused on the in-line geometry, which exhibits unsteady flow features distinctively different from those observed for normal triangle arrays. The parallel triangle array is then discussed and is shown to be more complex as its geometry combines features from the in-line and the normal triangle patterns. The last array to be considered is the rotated square geometry, whose flow characteristics have some similarities with those of normal triangle arrays. In general, the geometry of investigated bundles will be classified into small, medium and large tube spacings. This is because the flow development in each of these groups exhibits similar features. Finally, typical data of dynamic force coefficients and bound spectra of turbulent fluid forces on the tubes are given for selected cases.

2. Experimental Techniques

Two different types of tests were conducted to investigate different aspects of the flow field inside the bundle. The majority of bundles were investigated in a wind tunnel to allow the excitation of acoustic resonance. Thereafter, selected bundles were investigated in a water channel to facilitate flow visualization. During the water tests, favourable conditions were provided to stimulate self-excited resonance of free surface waves in order to be able to simulate the acoustic resonance observed in the wind tunnel. In the following, the main features of the air and water tests, together with the measuring technique are described.

2.1. Air Tests

The air tests were conducted in an open-circuit wind tunnel facility. The test-section was made of 10mm thick steel plates and had a cross-section of 200mm wide and a height of about 450mm. The upstream turbulence existing in the flow approaching the test-section was less than 1 %. An overall view of the test-section, for an in-line geometry, is shown in Fig. (1.4). Generally, both the pitch and the tube diameter were changed to obtain the required geometries with the maximum possible number of tubes in the test-section for a better representation of actual tube bundles. The tubes were made of acrylic rods and were rigidly fixed to the sidewalls of the test-section so that a modification of the flow structure through a coupling with the tube motion was avoided (Oengoeren & Ziada 1992b). Specially instrumented cylinders were used to measure the local pressure fluctuations on the tubes. A sketch illustrating this set-up is shown at the top of Fig. (2.1). The fluctuations were detected by connecting a microphone to a pressure tap 1 mm in diameter, drilled on the surface of the tube. In the preliminary tests, the spectra of the microphone measurements were compared with those of a hot wire located in the close proximity of the pressure tap for various flow velocities and it was verified that the pressure spectra measured with this set-up resemble the hot-wire spectra. The dynamic force measurements were made by means of the set-up shown at the bottom of Fig. (2.1). It is composed of a rigid cylinder and two piezo-electric transducers that are capable of measuring dynamic forces in the lift and drag directions simultaneously. This set-up is described in detail in Oengoeren & Ziada (1992b).

2.2. Water Tests

The water tests were carried out in a closed-circuit water channel facility. A closed surface insert test-section containing the tube array was utilized to avoid the effect of free surface oscillations. The streamwise turbulence level in the flow 20 tube diameters upstream of the first row was less than 0.1 %. The tubes were fixed vertically in the test-section. A more detailed description of the water test facility can be found in Oengoeren & Ziada (1992a). The resonance of the acoustic, transverse standing waves in the wind tunnel was simulated in the water tests by free surface waves in the transverse direction of the water channel. This was achieved by reducing the water level in the channel to allow free surface to form, but this was made only when the resonance mechanism was being investigated. The details of this technique including the analogy of these free surface

waves and acoustic resonances have been discussed in detail by Ziada & Oengoeren (1992, 1993). Dye injection technique was used to visualize the flow structure in the arrays. The images of the flow field were recorded by a video system. The photos presented in this paper were taken from the screen of the video system. Further details of the set-up and the experimental technique used in water tests can be found in Ziada & Oengoeren (1992, 1993) and Oengoeren & Ziada (1992a).

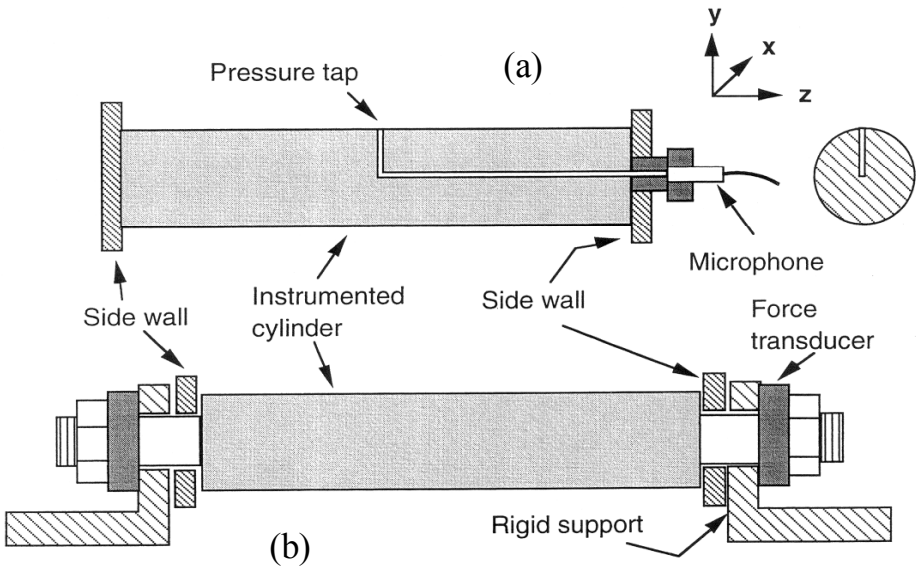

Figure 2.1. Sketches illustrating the instrumented cylinders used to measure local pressure (top) and dynamic forces (bottom) on the tubes of the array.

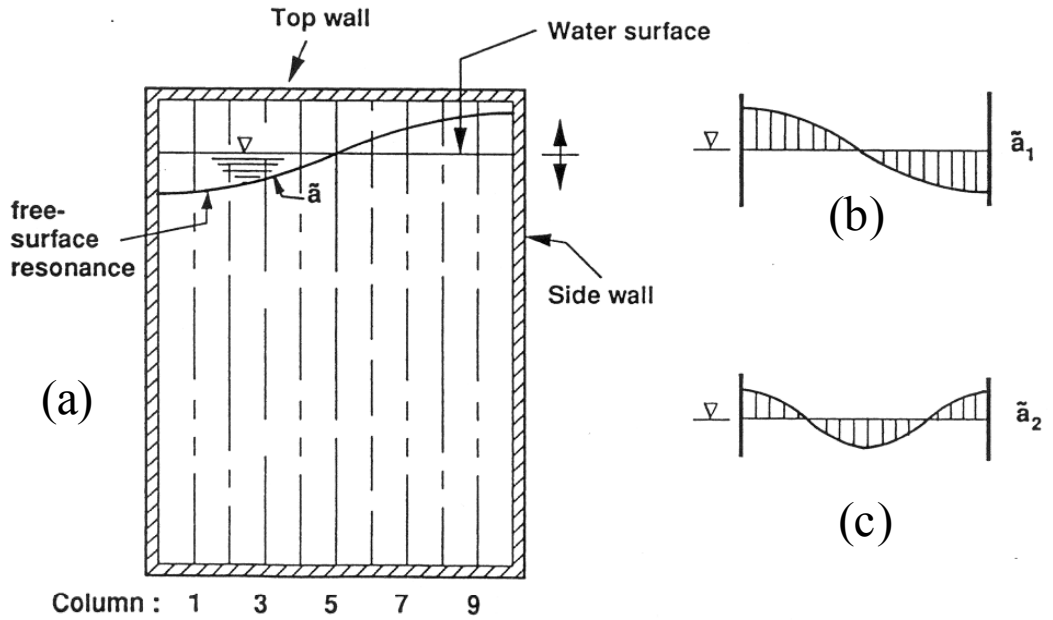

Figure 2.2. Sketches illustrating: (a) front few of the water channel test section in which the tubes are vertically mounted; (b) first mode shape of free surface wave resonance; (c) second mode shape of free surface wave resonance.

2.3. Instrumentation

The pressure fluctuations on the tubes as well as the SPL on the walls of the wind tunnel were measured by means of 1/4" condenser microphones. The velocity fluctuations, both in air and in water, were measured by means of a hot-film anemometer system. The capability of moving the microphones and the hot-film to any location within the arrays enabled extensive phase and coherence measurements which provided information about the spatial characteristics of the flow structure. Piezo-electric transducers were used to measure the dynamic forces on the tubes. The data acquisition and analysis were made either by a 16-channel computer or by a two-channel real-time analyser. Each spectrum obtained was an average of 50 samples in air tests. This number was increased to 100 in case of coherence and phase measurements. In the water tests, 20 samples were used.

3. Normal Triangle Tube Arrays

3.1. Overview of Flow Periodicity

Figure (3.1) shows a normal triangle array geometry for which the spacing (or pitch) ratio is defined as $X_p = P/d$. Typical pressure spectra for a small, an intermediate, and a large pitch ratio, X_p = 1.6, 2.08 and 3.41, respectively, are given in Fig. (3.2). For each case, spectra of rows 1-5 taken during air tests are illustrated. Three frequency components are observed at the first row for the cases X_p = 1.6 and 2.08 and two components are apparent in the case of X_p = 3.41. These components are referred to hereafter as f_{v2}, f_{vl} and f_{vd}, from the highest to the lowest, respectively.

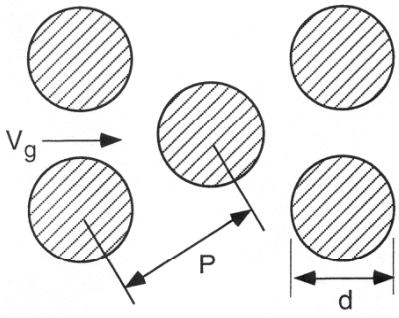

Figure 3.1. Relevant parameters of normal triangle array

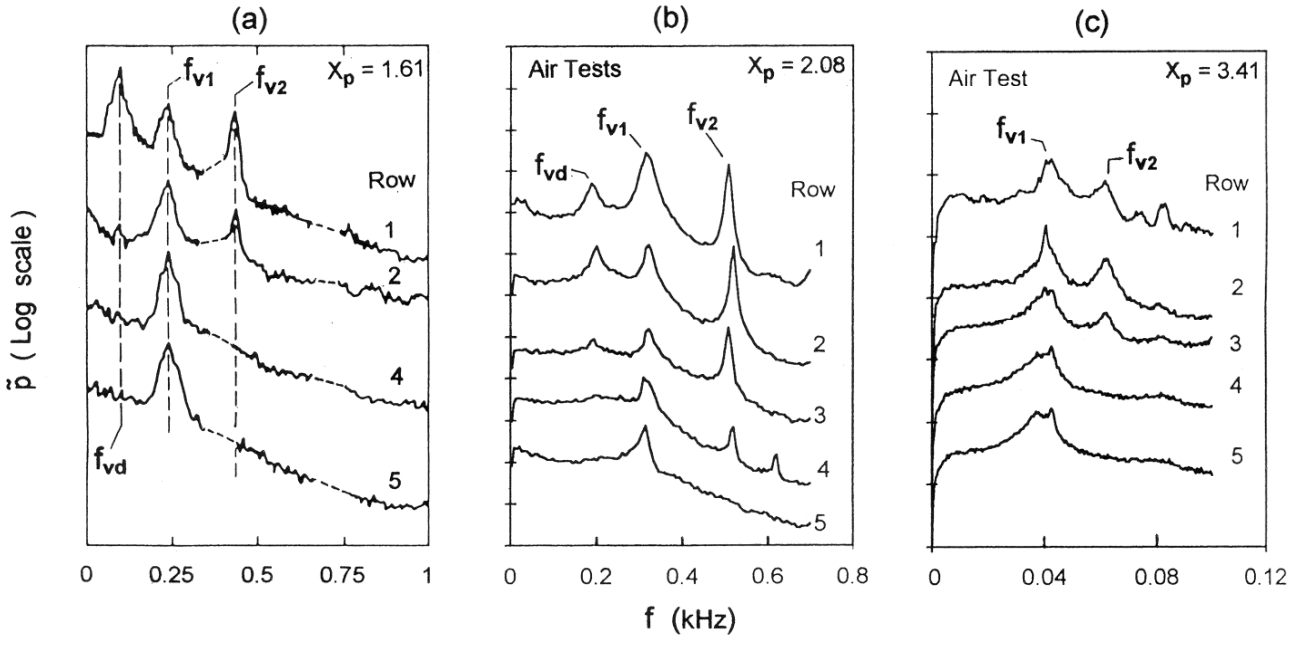

Figure 3.2. Typical pressure spectra measured at rows 1 to 5 and (a) on top wall of the wind tunnel, (b) and (c) on the tubes of **normal triangle arrays in air flow.** (a) *Xp*=1.61, R=49600; (b) *Xp*=2.08, R=26300; and (c) *Xp*=3.41, R=6000.

As observed in Fig. (3.2.a), which belongs to the small spacing ratio, the components f_{vd} and f_{vl} have relatively broader frequency bands as compared with the peak f_{v2}. The peak f_{vd} becomes hardly discernible at the second row. The peak f_{v2} also weakens substantially at the inner rows and totally disappears at row 4. Only the f_{vl} component is sustained at rows from 1 to 5. It should be mentioned at this point that the spectra for this case (X_p = 1.6) were measured with a microphone located on the top wall of the test-section. Therefore, the responses of the first and the second acoustic modes were also present in addition to the vortex-shedding peaks. These acoustic responses were removed from these spectra and replaced by dotted lines to avoid a possible confusion. The pressure spectra of the intermediate spacing case, Fig. (3.2.b), were measured by means of a microphone connected to a pressure tap on the tube, as shown in Fig. (2.1.a). They show similar characteristics as the small spacing case; however, the peak f_{v2} is stronger and is sustained somewhat deeper inside the array up to the fourth row. The pressure spectra of the large spacing array contain only two frequency components, f_{v1} and f_{v2}, at the first row. In contrast to the previous two cases, both components are rather broad-banded, even at the front rows. However, the development of these peaks towards the inner rows is similar to the other cases.

The frequency component f_{vd} appears to be relatively broad-banded and tends to disappear as one of the other peaks becomes weaker. In fact, a close look at the spectra of the intermediate spacing array shows that f_{vd} is exactly equal to the difference between f_{v2} and f_{v1} ($f_{vd} = f_{v2} - f_{v1}$). These features suggest that the component f_{vd} results from nonlinear interaction between f_{v1} and f_{v2}. This phenomenon of nonlinear interaction between different frequency components in separated flows has been reported by many researchers; see, for example, Miksad (1973). The f_{vd} component was studied carefully in all cases tested and it was verified that it stems from the interaction between the two components f_{v1} and f_{v2}, and not from another periodic flow structure.

The results presented in the foregoing illustrate that the flow activities in the three arrays exhibit some similarities. However, it should also be emphasized that these results are based on some rather selective data. These data were obtained utilizing different measurement techniques as well as different Reynolds numbers. An examination of the data provided in the literature for similar geometries shows that some of the features mentioned above have been overlooked because of differences in the test conditions, measurement techniques and/or the location of measurements. In order to establish a baseline for normal triangle tube arrays, the tests of each of the above geometries were carried out according to a standard procedure by Oengoeren & Ziada (1998). The objective was to study the effects of Reynolds number and row depth on the vortex-shedding process and the dynamic forces exerted on the tubes. In the following, these issues are discussed in some detail for intermediate tube spacing and then briefly for small and large spacing ratios.

3.2. Normal Triangle arrays with Intermediate Tube Spacing

3.2.1. Effect of Reynolds number on vortex shedding

In order to illustrate the effect of Reynolds number on the vortex-shedding phenomenon, the spectra of the pressure fluctuations on a tube in the second row and the spectra of the velocity fluctuations detected by a hot-film located behind rows 1 to 5 are given in Fig. (3.3). These measurements cover a Reynolds number range of 17300-52000. Only one vortex-shedding peak, f_{v2}, is observed at low Reynolds numbers (Re < 22200). It corresponds to a Strouhal number of 0.4. As the Reynolds number is increased to 22200, this peak becomes weaker and a second peak, f_{v1}, appears in the spectrum with a Strouhal number of 0.26. The peak f_{v1} is rather weak and broad-banded at this Reynolds number. With further increases in the Reynolds number, the enhancement in f_{v1} and the decrease in f_{v2} components continue. At a Reynolds number of 32000, the amplitude of f_{v1} becomes significantly stronger than f_{v2}. As this process of frequency change continues, a third

peak, $f_{vd} = f_{v2} - f_{v1}$, corresponding to a Strouhal number of 0.14 emerges in the pressure spectra for Reynolds numbers over 22200. It is interesting to note that the difference component f_{vd} reaches its strongest level at the second row and when both components f_{v1} and f_{v2} are relatively strong. The modulation of the frequency of vortex shedding behind row 2 vanishes when the Reynolds number is increased above 45000, where the vortex shedding transforms into a single-frequency event at the lower-frequency component f_{v1} (S = 0.26). A typical pressure spectrum measured in this range is given in Fig. (3.3.a) for Re = 52000. Similar pressure and hot-film measurements carried out on the first row showed that the same transformation also occurs behind this row. This means that the *vortex shedding phenomenon becomes a single-frequency event with a Strouhal number of 0.26 throughout the whole bundle in the high Reynolds number range.*

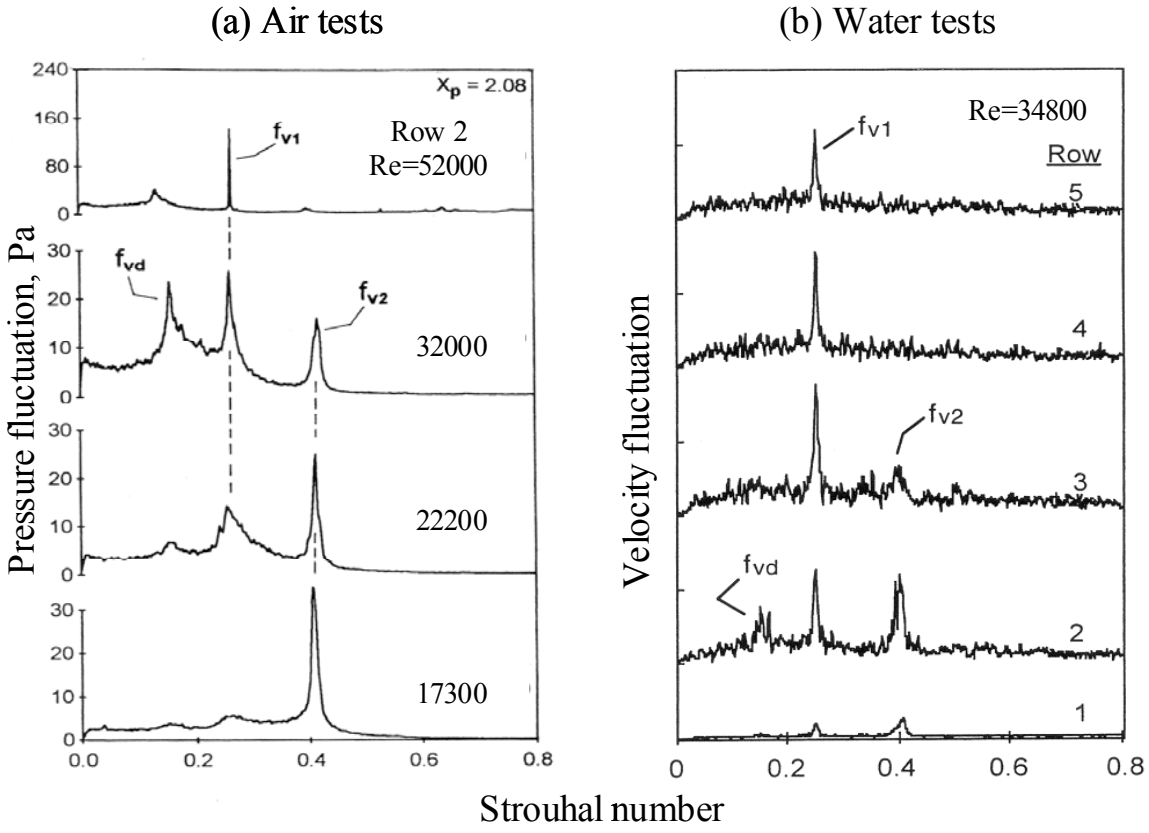

Figure 3.3. Spectra of (a) pressure fluctuations measured on a tube in the second row for different Reynolds numbers and (b) velocity fluctuations measured by a hot-film behind rows 1 to 5 of the intermediate spacing array (X_p = 2.08).

From the results presented in this section, it is clear that the multiple frequency nature of vortex shedding is strongly Reynolds number dependent. It is particularly interesting to note that the flow activities in this array transform into a single-frequency phenomenon with a frequency of f_{v1} in the Reynolds number range of Re > 50000.

3.2.2. Effect of row number on vortex shedding

Figure (3.3.b) shows the effect of row number at Re of 34800. Additionally, pressure spectra measured on the first five rows were previously presented in Fig. (3.2.b). As observed in these figures, the vortex shedding peaks f_{v1} and f_{v2} and the associated difference component f_{vd} exist in both pressure and velocity spectra in the front rows. The component f_{v2} becomes gradually weaker as one proceeds towards the inner rows and ceases to exist rather promptly after the third or fourth row. In contrast to f_{v2} the component f_{v1} exists in the spectra for the whole bundle at this particular Reynolds number range, being the only peak existing after the fourth row.

From the foregoing results, it may be suggested that data obtained in tube bundles having less than five rows may not be representative. At relatively low Reynolds numbers, the changes in the vortex-shedding behaviour might be displayed only partly in the results. On the other hand, measurements made solely on rows deeper than the fourth in deep tube bundles may not reflect all aspects of vortex shedding, either. In such cases, the multiple frequency nature of vortex shedding and its transformation to a single-frequency event may be overlooked.

3.2.3. Nature of vorticity shedding

In order to investigate the local and global characteristics of the vortex-shedding process that dominates over the whole bundle, the phase and the coherence distributions of the fluctuation velocity behind several rows were measured in detail as functions of the vertical distance, y. A diagram showing the measurement locations is given at the bottom of Fig. (3.4). A length of two vertical pitches was traversed behind rows 3, 5, 7 and 9 to account for the relation between the flow patterns in different columns as well as in different rows so that an overall spatial image of the flow structure could be obtained.

As shown in Fig. (3.4), the fluctuating pressure signal detected by means of a pressure tap located at the mid-span of a tube in the fifth row was used as a reference in all the coherence and phase measurements of the velocity fluctuations. The phase of the velocity fluctuations at the frequency component f_{v1} measured behind rows 3, 5 and 7 for a velocity of 21.2 m/s (Re = 25500), are plotted in Fig. (3.4.al). The positions y/P = 0, 1 and 2 correspond to the centrelines of the tube wakes. All the phase data of f_{v1} belonging to different rows produce a single distribution as observed in this figure. *This means that the flow structures behind the three rows are identical and synchronized* (because the associated phase distributions are similar and are also in phase with each other). Moreover, the data belonging to neighbouring tube wakes (or flow lanes) have identical distributions, e.g. the phase distribution in flow lane 11 is identical to that in flow lane 12. This indicates that the flow pattern is identical and synchronized in the wakes of neighbouring tubes in each row. These rather remarkable features illustrate the fact that the flow patterns in the wakes of all tubes in rows 3, 5 and 7 are identical and synchronized. This flow pattern is identified as alternating vortex shedding from the tubes when the phase in each tube wake is examined (a phase jump of 180º occurs at the centre of each wake).

The coherence distributions associated with the aforementioned phase distributions are given in Fig. (3.4.a2). The distributions belonging to all rows are similar. The coherence drops to a minimum at the centres of the tube wakes and the flow lanes, where a phase jump occurs because the vortices at the opposite sides of these locations have opposite circulations, see the diagram at the bottom of Fig. (3.4). The coherence increases rapidly away from these locations, because the velocity fluctuations become better defined, and it reaches a maximum of 0.75. A high coherence between the velocity fluctuations at different locations indicates that these fluctuations are associated with the same (global) flow phenomenon. The phase and coherence measurements were repeated for rows 5, 7 and 9 at a higher velocity of 33 m/s (Re = 39600) in order to verify this very organized flow behaviour. The results are given in Fig. (3.4.b). All the characteristics of the previous low Re case are evident also in this case, indicating that the same flow structure exists at high Reynolds numbers. Additionally, a significant enhancement is observed in the coherence level at this velocity, reaching a maximum of 0.98 in comparison with a level of 0.75 in the low velocity case. Both cases are clearly away from the range of acoustic resonance (Oengoeren & Ziada, 1998). Therefore, this globally synchronized flow structure cannot be attributed to a coupling mechanism with acoustic standing waves, but rather to a fluid dynamic mechanism that gains in strength as the Reynolds number is increased. The impingement of the shed vortices on the downstream cylinders may well be the source of the fluid dynamic mechanism that enhances this global mode of vortex shedding; for more details see Rockwell & Naudascher (1979).

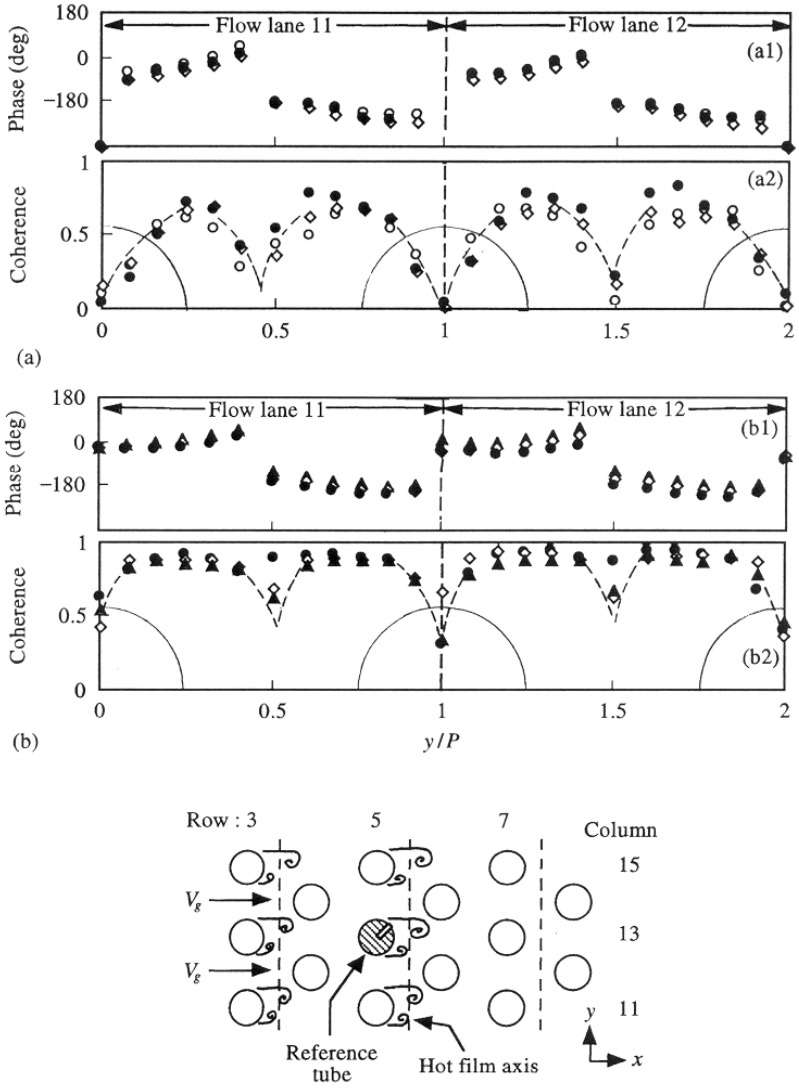

Figure 3.4. Distributions of phase and coherence of velocity fluctuations at f_{vl} for velocities of (a) 21.2 m/s (Re = 25500) and (b) 33 m/s (Re = 39600) behind rows 3, 5, 7 and 9. The pressure fluctuation on a tube located in the fifth row was taken as the reference signal for all measurements. Air tests: ○, row 3; ●, row 5; ◊, row 7; ▲, row 9.

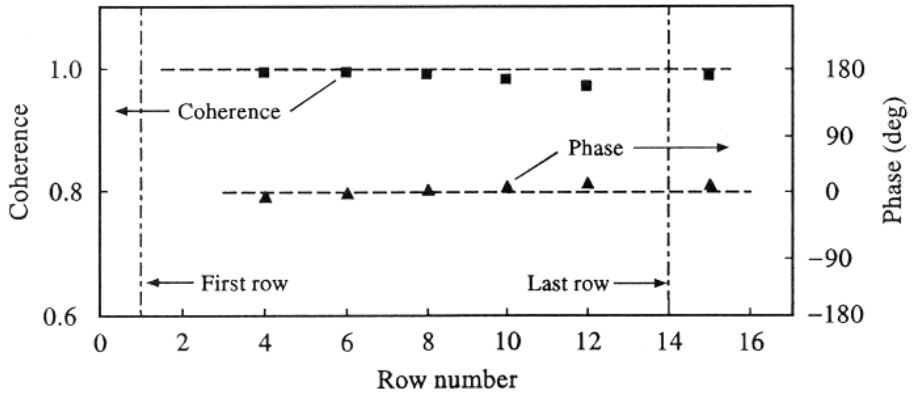

Figure 3.5. Distributions of coherence and phase of vortex-shedding component f_{vl} as functions of row depth at a velocity of 22 m/s (Re = 26400). The signal of row 2 was taken as the reference signal for all other rows.

Finally, Fig. (3.5) shows the coherence and the phase difference between the second and the deeper rows for the vortex shedding component f_{v1}. These results were obtained by means of two microphones located on the top wall of the test-section. It is seen that the vortices shedding from all rows are correlated and are in phase with each other implying a total synchronization of vortex shedding in the bundle.

3.2.4. Flow visualization

The flow visualization study was carried out in the water channel as described in Section (2). First, the frequency of vortex shedding was measured when the free surface in the test-section was covered, thereby precluding the formation of free-surface waves. The results of Strouhal number obtained by means of a hot film located at different rows were found to be similar to those obtained from the air tests (for more details see Oengoeren & Ziada, 1998).

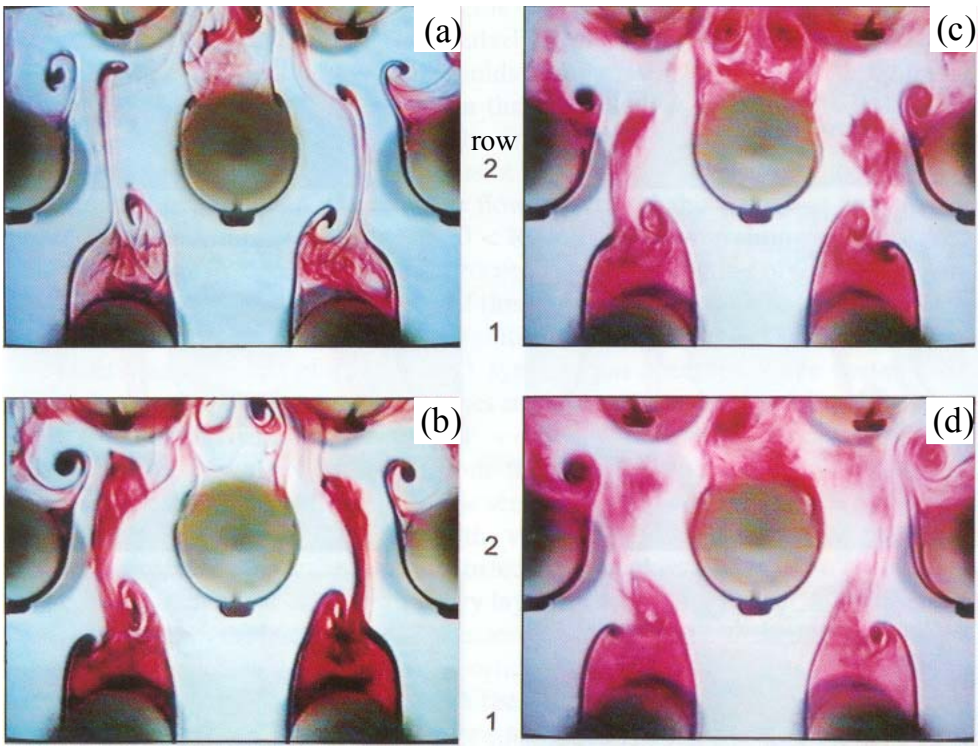

Figure 3.6. Flow structure behind the first two rows of an intermediate spacing normal triangle tube bundle (X_p = 2.08; d = 25 mm) in water for Reynolds numbers of (a) 1000, (b) 1800, (c) 5000, and (d) 7000.

A series of typical flow visualization photographs are given in Fig. (3.6), showing the flow structure behind the first and the second rows in a Reynolds number range of 1000 < Re < 7000. Alternating vortices are shed from the tubes of the first row. They then proceed into the flow lanes of the second row and promote vortex formation from the tubes of this row. The same flow pattern is observed in all the photographs despite the large range of Reynolds number. Symmetry is observed in the vortex-shedding pattern with respect to the centre of the tubes in the second row. However, this symmetric pattern occurs only intermittently and the flow switches to an antisymmetric mode as well. The mechanism of vortex shedding from the tubes of the first two rows is further delineated in Fig. (3.7), which shows the time series of the symmetric and the antisymmetric patterns for a Reynolds number of 1800. As the vortices in the wakes of the first tube row are convected downstream, they become distorted and weaker. When they reach the gap between the second row tubes, the boundary layers of these tubes erupt and form vortices; see the top left photograph of Fig. (3.7). These vortices remain attached to the tubes while being formed and then join the approaching vortices from the first row to form mushroom-shaped vortex pairs,

which finally impinge on the third row tubes. Downstream of the third row, the flow activities do not seem to have any organized nature at this Reynolds number.

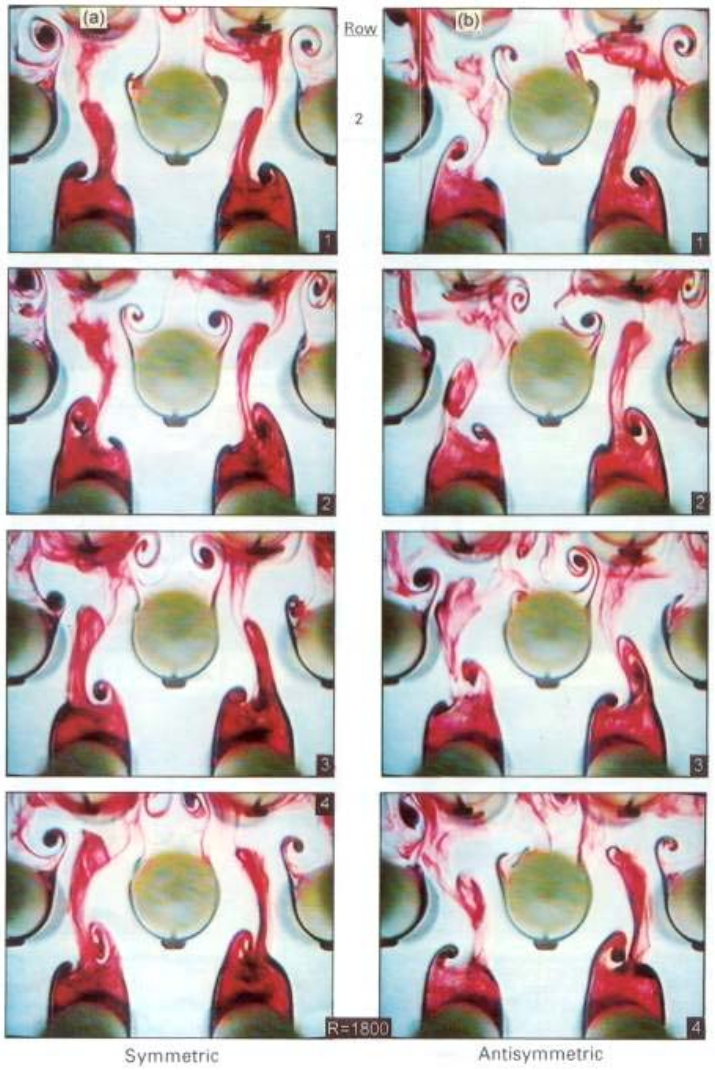

Figure 3.7. Time sequence of the two transient modes of vortex shedding behind the first two rows of the intermediate spacing normal triangle array for Re = 1800. Water tests; X_p = 2.08; d = 25 mm; (a) symmetric and (b) antisymmetric pattern of vortex shedding.

As can be seen from the time series of Fig. (3.7), the pattern of vortex shedding from the tubes in the *second* row depends on the phase between the two upstream wakes. Symmetric vortex shedding occurs when the upstream wakes oscillate out of phase. This symmetric shedding from any tube in the second row is out-of-phase with that of the neighbouring tubes; see the symmetric time series in Fig. (3.7). Antisymmetric vortex shedding from the second row tubes takes place when the upstream wakes oscillate in phase; see Fig. (3.7.b). It is noteworthy that the symmetric pattern was much more persistent than the antisymmetric one. These results suggest that vortex shedding from the first and the second rows occurs at the same frequency, which is the high-frequency component f_{v2}. This was confirmed by counting the frequency on the video monitor.

In order to show the vortex shedding pattern at high Reynolds numbers, where a single-frequency vortex shedding phenomenon occurs, the flow was visualized inside an array of larger diameter tubes. With this arrangement, the visualization of the flow at a Reynolds number of 35500 was possible. As shown in Fig. (3.8), a persistent alternating vortex shedding was observed behind the third row. Most importantly, counting of these vortices on the video has shown that they

correspond to the frequency component f_{v1}, which is in agreement with the hot-film spectra measured behind this row. A pattern belonging to f_{v2} component has not been observed in the flow visualization photographs taken behind this row at this Reynolds number.

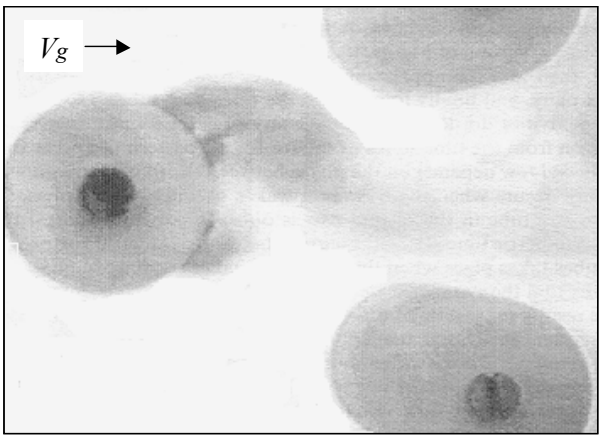

Figure 3.8. Alternating vortex shedding behind row 3 of a normal triangle array. X_p= 2.08; d=60mm; Re= 35500.

3.3. Normal Triangle Arrays with Large Tube Spacing

3.3.1. Effect of Reynolds number on vortex shedding

The effect of Reynolds number on vortex shedding in a widely spaced normal triangle array (X_p= 3.41) is illustrated in Fig. (3.9). Typical spectra of the velocity fluctuations behind the second row measured in airflow are given in Fig. (3.9.a). The two frequency components appearing in these spectra are called f_{vl} and f_{v2}, according to the definitions of these components in Fig (3.2). There are three Reynolds number ranges where different vortex shedding characteristics are observed. At low Reynolds numbers, Re < 6600, both f_{vl} and f_{v2} exist and follow the Strouhal number lines 0.2 and 0.28, respectively. In this range, the f_{v2} component is significantly weaker and has a relatively broader band than f_{vl}. At high Reynolds numbers, Re > 18200, only the vortex-shedding component f_{vl} remains in the spectra. In fact, this component becomes narrower and stronger as the Reynolds number is further increased. The spectra belonging to the range of 6600 < Re < 18200, show that vortex shedding changes from a multi-frequency to a single-frequency phenomenon. Within this transition range, the vortex-shedding component f_{v2} is gradually shifted towards the component f_{vl} as the Reynolds number is increased. The transition is completed as f_{v2} unites with f_{vl}. To illustrate this process better, the Strouhal numbers of both components are plotted as functions of the Reynolds number in Fig. (3.9.b), including both the air-and water-test data. The shift of f_{v2} towards f_{vl} is depicted clearly in this plot. Although the flow velocity in the air tests is about two orders of magnitude higher than that in the water tests, the transition range in both cases occurs at the same Reynolds number.

3.3.2. Effect of row number on vortex shedding

As in the previous case, similar measurements of the flow activities in a range of 6600 < Re < 26300 (Oengoeren & Ziada, 1998) showed that at the lower end of this range the vortex shedding has a multi-frequency nature containing peaks at f_{vl} and f_{v2} behind the first three rows. However, the peak f_{v2} disappeared after the fourth row, leaving f_{vl} as the only peak existing. This result suggests that the multi-frequency character of vortex shedding is confined not only to low Reynolds numbers but also to the upstream rows.

On the other hand, the single-frequency phenomenon appears behind all rows at the higher end of the Reynolds number range, with a frequency of f_{vl}. Although this result is expected for the inner rows in accordance with the results of the previous case, it is interesting to note that, at high

Reynolds numbers, vortex shedding from the first row becomes a single-frequency phenomenon and occurs at the low-frequency component f_{vl}. This trend is similar to that observed for the intermediate spacing case; however, it starts here at a substantially lower Reynolds number.

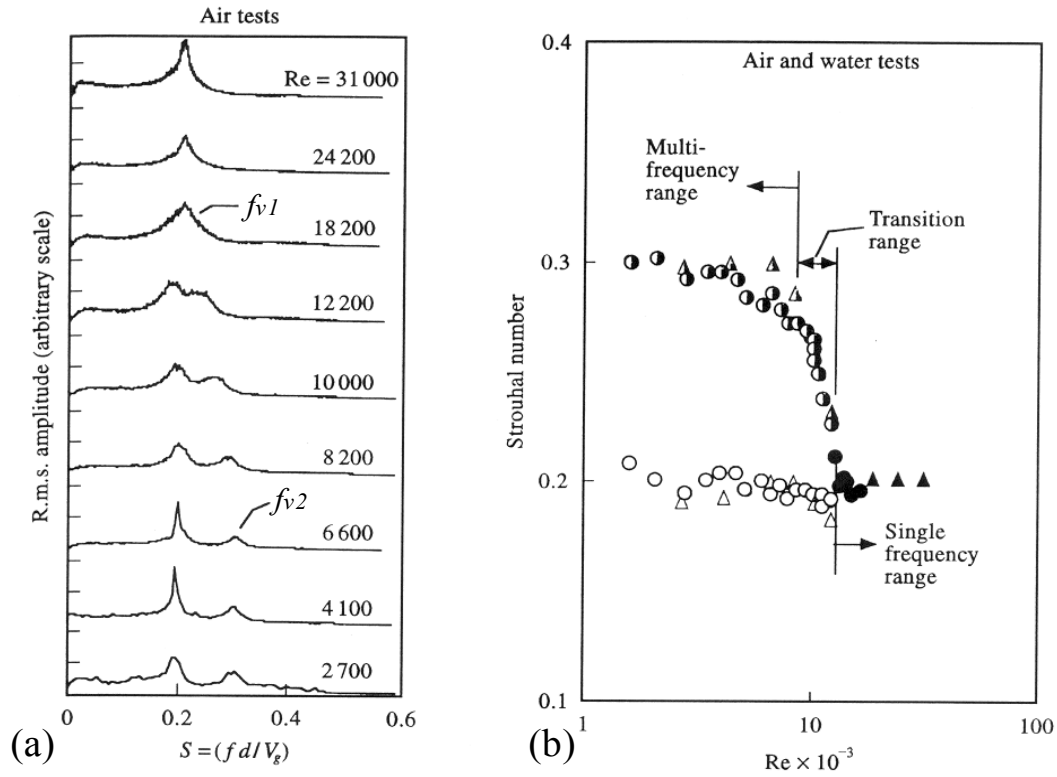

Figure 3.9. Transition process of frequency components in the large spacing array (Xp = 3.41).
(a) Frequency spectra of velocity fluctuations measured behind the second row in air, and
(b) strouhal number of vortex shedding measured in air and in water for 2700 < Re < 31000.
△, ◭, ▲, Air tests; ○, ◑, ●, water tests.

3.3.3. Flow structure

The photograph given in Fig. (3.10) depicts typical flow structures behind the first two rows of the large spacing array for a Reynolds number of 4800. Well-defined alternating vortices are shed from almost every tube of these rows. At this Reynolds number, the dominance of an antisymmetric mode of flow pattern is evident. Moreover, this mode is persistent for all times and a switch to a symmetric mode does not occur. The frequency of vortex shedding from the first two rows was counted from the video monitor. Vortex shedding from the first row occurred at the high-frequency component f_{v2}, but that from the second row occurred at the low-frequency component f_{v1}. Weaver et al. (1993) reported similar observations for rotated square arrays; i.e., the first-row shedding occurs at f_{v2} and that in the second row at f_{v1}. Since the transverse gap of rotated square arrays is larger than that of normal triangle arrays with similar pitch ratios, the first-row vortices interact less with the second-row tubes, and hence vortex shedding from the first two rows at different frequencies is more likely in rotated square arrays. It is therefore logical to see similar features in normal triangle arrays when the pitch ratio is sufficiently increased. The air-test results of this large spacing array have shown that a single-frequency vortex shedding sets in at Reynolds numbers higher than approximately 12000. By utilizing another test-section with larger diameter tubes, d = 31 mm, the Reynolds number range was increased over 12000 in order to visualize this single-frequency structure. In Fig. (3.11), the flow structure behind the first three rows is shown for a Reynolds number of 13800. There exist not only well-defined vortices behind the tubes of at least the first three rows, but they also seem to shed in phase with each other. By means of hot-film

measurements and video counting, these vortices were found to have a shedding frequency corresponding to the lower vortex-shedding component f_{v1}. It should be noted that the hot-film signal was superimposed on the video screen and then used as a timer to piece together the photographs shown in Fig. (3.11).

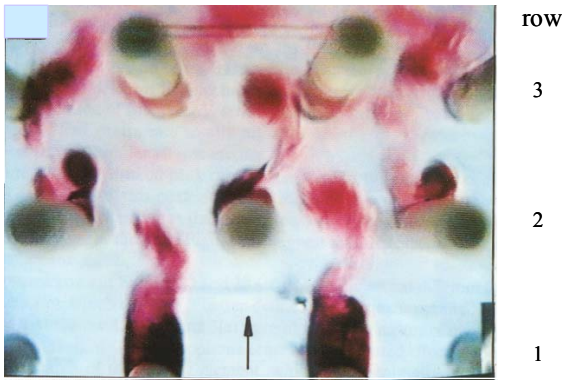

Figure 3.10. Typical flow patterns behind the first two rows of a large spacing normal triangle array for Re = 4800; X_p = 3.41, d = 16mm.

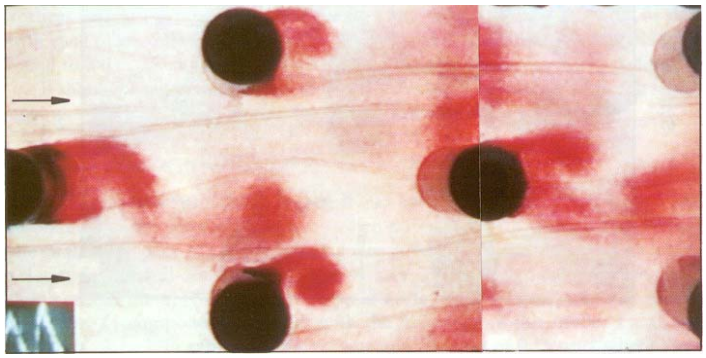

Figure 3.11. Overall view of the flow structure in a large spacing normal triangle array for Re=13800; X_p = 3.41, d = 31mm.

3.4. Normal Triangle Arrays with Small Tube Spacing

3.4.1. Nature of vorticity shedding

Typical spectra of pressure fluctuation on rows 1-4 of a small spacing normal triangle array (X_p=1.61) are given in Fig. (3.12) for a Reynolds number of 53300. A narrow-band peak at a Strouhal number of approximately 0.6 is clearly seen in the spectra. This Strouhal number, which corresponds to the vortex-shedding component f_{v2}, is very close to that measured for the same geometry by Zukauskas & Katinas (1980). The background turbulence level increases gradually as the flow progresses into the bundle; however, no other distinct peaks that can be attributed to periodic flow activities can be seen in these spectra. A broad-band peak can be seen at a Strouhal number of about 0.15. Despite its broad-band nature, this peak does not seem to be generated by the turbulent buffeting mechanism because it exists at the second row only and within a certain range of Reynolds number.

The pressure spectra given in Fig. (3.12) seem to be somewhat different from those presented in Fig. (3.2.a), which displays a better-defined low-frequency component, f_{vl}. It should be recalled that the results of Fig. (3.2.a) were obtained by means of a microphone on the top wall of test section.

This microphone senses the integrated effect of the pressure fluctuations over the area of the sensing element, which is substantially larger than the pressure taps on the tubes. The enhancement of the peak at f_{vl} in the microphone signal is therefore attributed to an improved coherence and correlation length of the pressure fluctuation at this frequency. Undoubtedly, the low-frequency component f_{vl} becomes weaker, broader and develops at higher Reynolds number in this small spacing array. It seems to be associated with the development of the flow turbulence at the downstream rows.

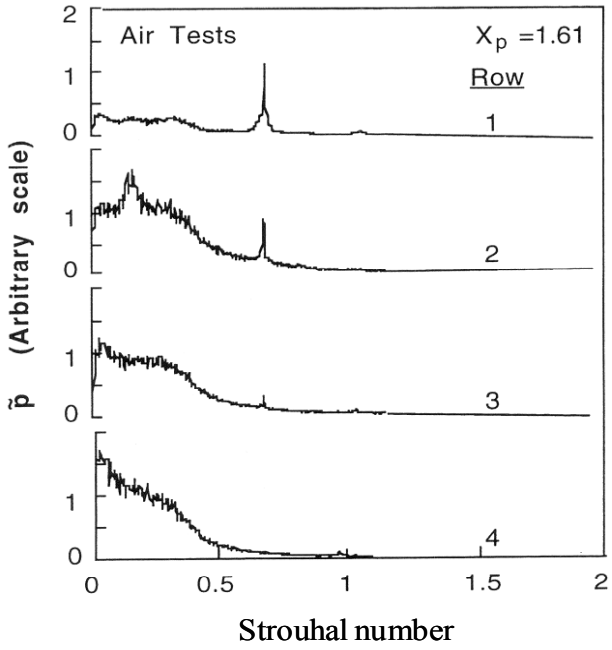

Figure 3.12. Spectra of pressure fluctuations on the tubes of rows 1 to 4 at Reynolds number of Re = 53300. Air tests of a normal triangle array with small spacing ratio; $X_p = 1.61$

3.4.2. Flow structure

Figure (3.13.a) displays the flow structure behind the first three rows at Reynolds number of 3050. Well-defined but relatively weak vortices are shed behind the first row. They become rather strong behind the second row despite their relatively small scale. However, they are diffused at the third row, and vortex-like structures totally disappear downstream of this row. As in the case of intermediate spacing, alternating vortex shedding occurs behind the first row and symmetric vortices are shed from the second row. This pattern does not seem to be intermittent in this array, as opposed to the observations of the intermediate and the large spacing arrays. The flow structure was observed to remain the same when the Reynolds number was increased up to 15250, Fig. (3.13.b). The video counting of the frequency of vortex shedding from rows 1 and 2 verified that they are f_{v2} vortices and correspond to the Strouhal number $S_2 = 0.55$.

3.5. Acoustic Resonance of Normal triangle arrays

Since the vortex-shedding frequency increases linearly with the flow velocity, it may coincide with the frequency of an acoustic mode. Near the condition of frequency coincidence, powerful acoustic resonances may be produced. The acoustic modes of interest are those consisting of standing waves in a direction normal to the flow and the tube axis. As shown in Fig. (1.4), the first acoustic mode, f_{a1}, consists of half a wavelength ($\lambda/2$) and the second, f_{a2}, constitutes a full wavelength (λ) between the top and the bottom walls of the wind tunnel.

A typical example for normal triangle arrays is illustrated in Fig. (3.14), which shows the acoustic response of a large spacing array with X_p=3.41. An acoustic resonance is initiated as the

vortex-shedding frequency f_{v1} coincides with the first acoustic mode frequency, f_{a1}, at a velocity of 42 m/s. A lock-in of the vortex- shedding frequency with the acoustic resonance frequency occurs in the velocity range of 42-51 m/s. Within this range, the SPL increases rapidly until it reaches a level of 156dB.

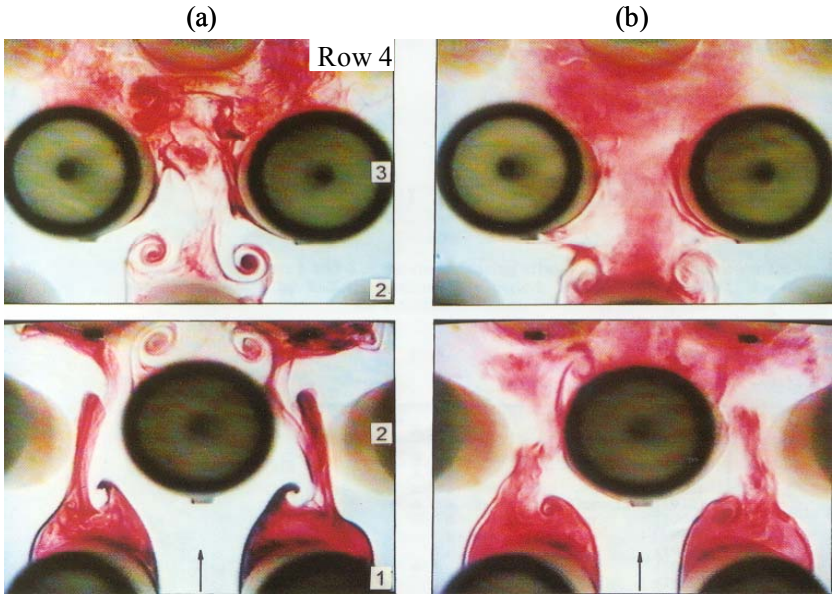

Figure 3.13. Typical flow patterns behind rows 1-3 for Reynolds numbers of (a) Re = 3050 and (b) Re = 15250 in a small spacing normal triangle array. X_p = 1.61, d = 60mm.

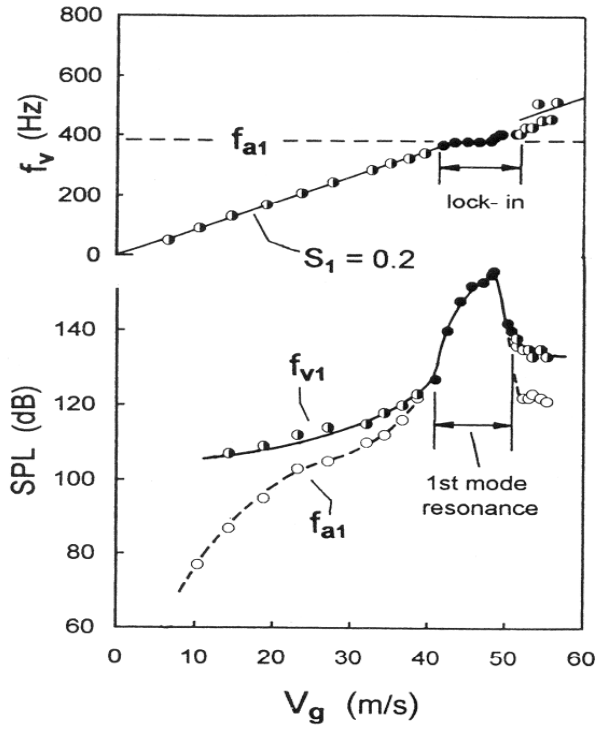

Figure 3.14. Sound pressure level (SPL) of the vortex shedding component f_{v1} and the first acoustic resonance mode f_{al}, and the corresponding frequency distributions as functions of gap velocity V_g in a large spacing normal triangle array.

It should be noted that in this particular case of large spacing, the higher vorticity shedding component, f_{v2}, did not excite acoustic resonance. The ability of this component to excite acoustic resonance increases substantially as the tube spacing ratio is decreased. In fact, for the other tube spacings discussed above, X_p = 1.61 and 2.08, the acoustic modes were excited by the vortex shedding component f_{v2} (for further details see Oengoeren and Ziada, 1998). For this reason, design against acoustic resonance should be based on the fact that both vorticity components are capable of exciting acoustic modes.

3.6. Strouhal Numbers of Normal Triangle Tube Arrays

The Strouhal numbers of the main components of vortex shedding in normal triangle arrays are given in Fig. (3.15). A particular criterion was not set in the selection of the data points and, therefore, some of them may not be reliable because they were extracted from either tube or acoustic resonances. However, the results of the three arrays discussed above indicate that *the Strouhal numbers at the onset of acoustic resonances in normal triangle arrays approximate those of the natural vortex shedding away from resonance conditions.* Thus, the use of these data to construct a chart of Strouhal numbers for normal triangle arrays seems to be justified. For the sake of clarity, the non-linear interaction component f_{vd} is not included in the Strouhal number chart. This is because this component does not seem to cause any "harmful effects", at least within the tested ranges of spacing ratios and Reynolds numbers. The Strouhal number given in Fig. (3.15) is defined as:

$$S = f_v \, d/V_g \tag{1}$$

where f_v is the shedding frequency, d is the tube diameter and V_g is the gap flow velocity.

As expected, the data gather around two Strouhal number lines, S_1 and S_2. The points on the line S_2 correspond to the vortex shedding component f_{v2}, which is observed mainly behind the front rows. However, at high Reynolds numbers, this component may totally disappear in bundles with intermediate and large spacing ratios (X_p > 2). Increasing the spacing ratio results in a reduction in the Reynolds number at which this high-frequency component disappears.

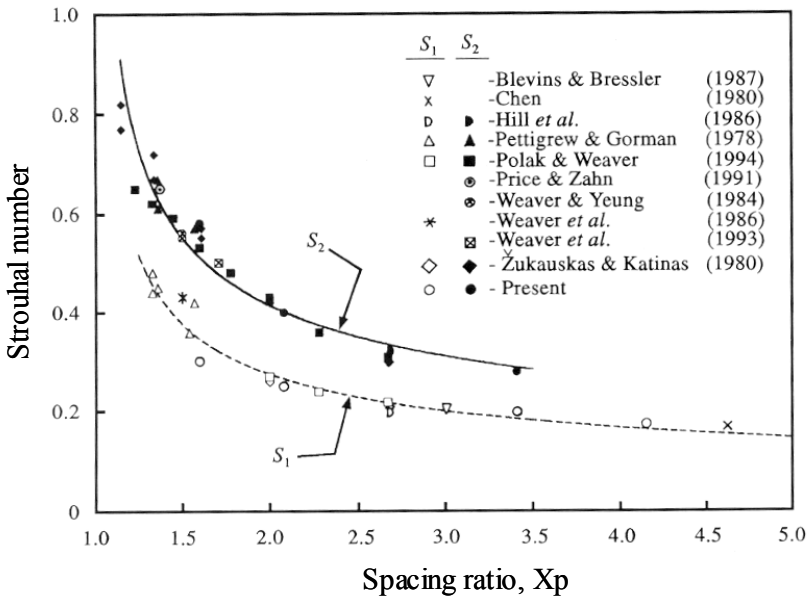

Figure 3.15. Strouhal number data of vorticity shedding components in **normal triangle arrays** as function of the spacing ratio. Refer to Oengören & Ziada (1998) for data sources.

The line S_1 belongs to the frequency component f_{v1}. This component has the characteristics of turbulent buffeting excitation for small tube spacings ($X_p \sim 1.6$); however, it is associated with well-defined vortex shedding at the inner rows for larger tube spacings ($X_p > 2$). Moreover, it becomes the only flow periodicity existing in bundles with large spacing ratios and at high Reynolds numbers. The range of Reynolds number over which this component becomes dominant depends on the particular spacing ratio.

Whether acoustic resonances of normal triangle arrays are excited by f_{v1}, f_{v2} or both depends on the spacing ratio. For spacing ratios of less than about 1.7, acoustic resonances are liable to the high-frequency component, f_{v2}. The lower modes, however, may not be excited because the frequency coincidence occurs at low dynamic heads where the vorticity shedding excitation may still be weak in comparison to the system acoustic damping. Several acoustic damping criteria have been developed by Chen (1968), Fitzpatrick (1986), Ziada et at. (1989b), Blevins & Bressler (1992) and Eisinger et at. (1992).

In the range of intermediate spacing ratios, $1.8 < X_p < 2.7$, either frequency component can excite acoustic resonances. However, those excited by the high-frequency component are generally weak, whereas those excited by the lower component are very strong and can be destructive. Other researchers (e.g. Blevins & Bressler, 1987a, b) also suggested that the higher component excites the lower modes only weakly, if at all. At high Reynolds numbers, the low component f_{v1} becomes the only relevant excitation anyway.

Acoustic resonances of large spacing arrays, $X_p > 2.8$, are excited by the lower-frequency component only. Since the higher component exists only at low Reynolds numbers and appears only at the first row or two, the fluctuating energy associated with it is presumably too small to excite resonances.

The boundaries between small, intermediate and large spacing ratios are obviously not as well-defined as might be suggested by the above. Those boundaries selected above are based on the results of a limited number of experiments. Future tests on additional geometries near these boundaries would improve our knowledge of which Strouhal number is more relevant in these transition regions.

An important feature of normal triangle arrays is that acoustic resonances are excited by the vorticity-shedding excitation that dominates before the onset of resonance. This implies that the Strouhal number charts of vorticity shedding can be used to design against acoustic resonances. In order to provide a better prediction means of Strouhal number, empirical forms of S_1 and S_2 have been obtained from the least-squares approximation of the data points in Fig. (3.15) and are given by the formulae:

$$S_1 = \frac{1}{3.62(X_p - 1)^{0.45}} \quad , \quad S_2 = \frac{1}{2.4(X_p - 1)^{0.41}} \tag{2}$$

These empirical lines are shown in Fig. (3.15).

3.7. Summary of Results for Normal Triangle Tube Arrays

1. Three distinct frequency components of vortex shedding, f_{v1}, f_{v2} and f_{vd}, are observed. The components f_{v2} and f_{v1} ($f_{v2} > f_{v1}$) are found to be associated with alternating vortex shedding from the tubes in the front and the rear rows, respectively. The third component, $f_{vd} = f_{v2} - f_{v1}$, seems to result from the non-linear interaction of f_{v1} and f_{v1}, and is observed in the transition region (mostly behind the second row) where both components f_{v1} and f_{v2} coexist.
2. The nature of vortex shedding and the relative importance of each frequency component depend on the spacing ratio, the Reynolds number, the location within the array and, in some cases, on the number of rows and the number of tubes in each row.
3. Based on the general characteristics of vorticity shedding, normal triangle tube arrays are classified into small, intermediate and large spacing categories.

4. In the intermediate spacing case, both components of vortex shedding can be strong. However, the lower component f_{v1} develops over the whole depth of the array at high Reynolds numbers. The mechanism that enhances this component at high Reynolds numbers is believed to be of a fluid dynamic nature such as that described by Rockwell & Naudascher (1979).
5. Increasing the spacing ratio weakens the high-frequency component f_{v2} at the front rows, until the lower-frequency component f_{v1} dominates also at the front rows. The opposite occurs when the spacing ratio is reduced, however, the component f_{v2} remains confined to the front rows only.
6. In general, acoustic resonances of normal triangle arrays occur in a *classical manner* such that the onset of resonance is initiated when the frequency of natural vortex shedding approaches the resonance frequency. The Strouhal number charts of vorticity shedding can therefore be used to design against acoustic resonances.
7. The relative importance of the vorticity shedding components f_{v1} and f_{v2} with respect to the excitation of acoustic resonances is clarified and is related to the proposed classification of spacing ratios.
8. A Strouhal number chart for vorticity shedding excitation is developed and empirical forms are proposed to predict the Strouhal numbers over a wide range of spacing ratios.

4. Rotated Square Tube Arrays

The main flow characteristics of rotated square arrays are similar to those of normal triangle arrays, which are discussed in detail in the previous section. For this reason, only a brief summary of rotated square arrays is given here. The majority of the results reported in this section are from Weaver et al. (1993).

Figure (4.1) shows the main parameters of the rotated square layout geometry. As in the previous case, the spacing (or pitch) ratio is defined as $X_p = P/d$. *In this section only, all flow parameters, including the Strouhal number, are given in terms of the upstream flow velocity, V_u , which is the free stream velocity upstream of the bundle.*

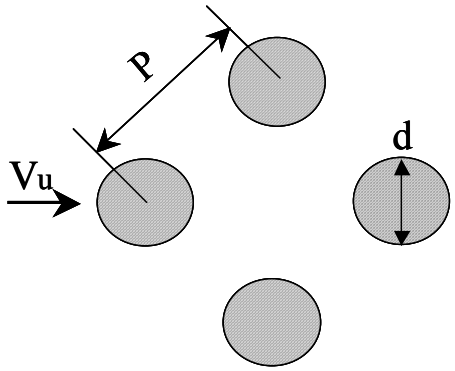

Figure 4.1. Definitions of rotated square layout of tube bundles

4.1. Vorticity Shedding Excitation

Weaver et al. (1993) observed two Strouhal numbers in rotated square arrays. Figure (4.2) shows two frequency spectra, the first measured behind the first row and the second behind the third row. As can be seen, the higher frequency component of vortex shedding (5.8 Hz) is generated at the upstream rows. In fact, Weaver et al. reported that this component is caused by alternating vortex shedding from the first row as can be seen from the flow visualization picture in Fig. (4.3.a). This component becomes weaker as the flow progresses downstream and it subsides totally by the third row as shown in Fig (4.2.b). On the other hand, the low frequency component of vortex shedding (3.7 Hz) becomes stronger at the downstream rows and is related to vortex shedding behind other rows as shown in Fig. (4.3.b) which shows alternating vortex shedding behind the second row at the low frequency component. No other frequency components are observed in this case.

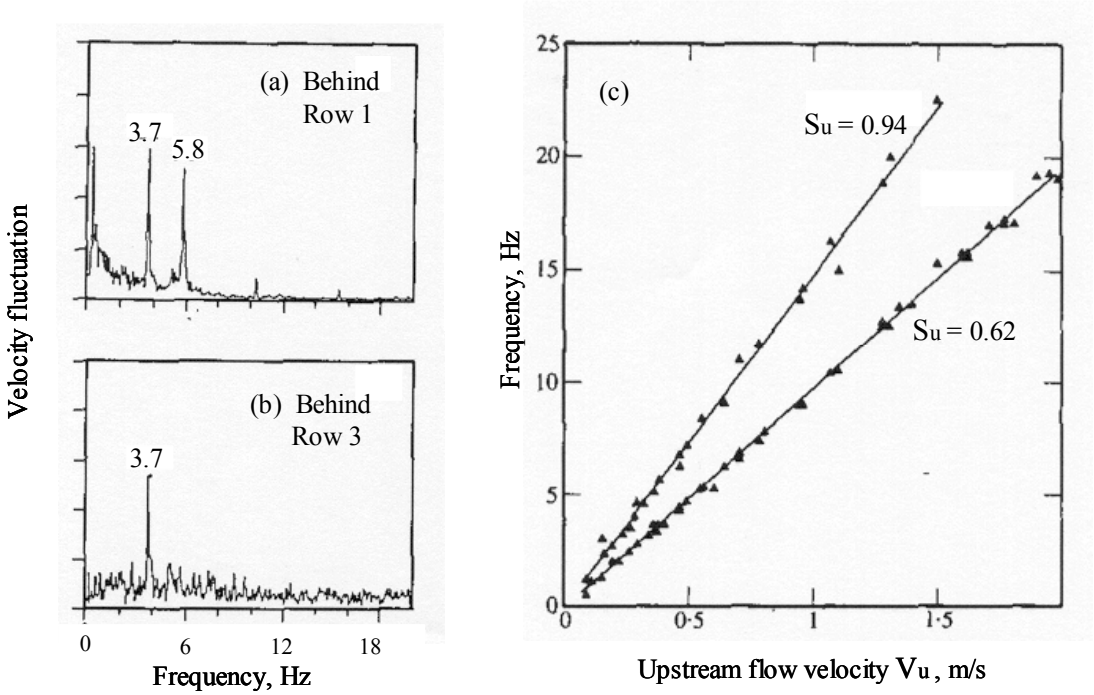

Figure 4.2. Rotated square array results: (a & b) Velocity spectra behind the first and third rows, respectively; (c) frequencies of vorticity shedding as function of upstream flow velocity showing two Strouhal numbers. X_p = 1.7; from Weaver et al. (1993).

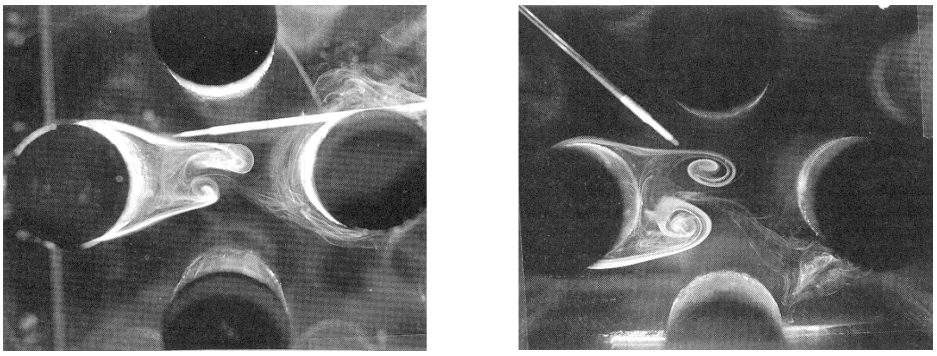

(a) Vortex shedding behind first row (b) Vortex shedding behind second row

Figure 4.3. Flow visualization pictures for rotated square array: Vortex shedding behind a tube (a) in the first row and (b) in the third row. X_p = 1.7; $Re_u \approx 950$; from Weaver et al. (1993).

4.2. Strouhal Number Chart for Rotated Square Arrays

Figure (4.4) depicts the Strouhal number of vorticity shedding as a function of the pitch ratio X_p. It is important to recognize that this Strouhal number S_u is based on the upstream flow velocity (V_u):

$$S_u = f_v \, d/V_u \tag{3}$$

where, f_v is the vortex shedding frequency, d is the tube diameter, and V_u is the flow velocity upstream of the array.

The data points in Fig. (4.4) are seen to collapse on two Strouhal number lines. The higher corresponds to vortex shedding from the first row, and the lower is caused by vortex shedding from other rows. As expected, the Strouhal number decreases when the pitch ratio is increased.

Results in the literature indicate that acoustic or tube resonance can be excited by either of the Strouhal numbers documented in Fig. (4.4). It is therefore recommended to use Fig. (4.4) for design purposes in order to assess the possibility of acoustic or tube resonance.

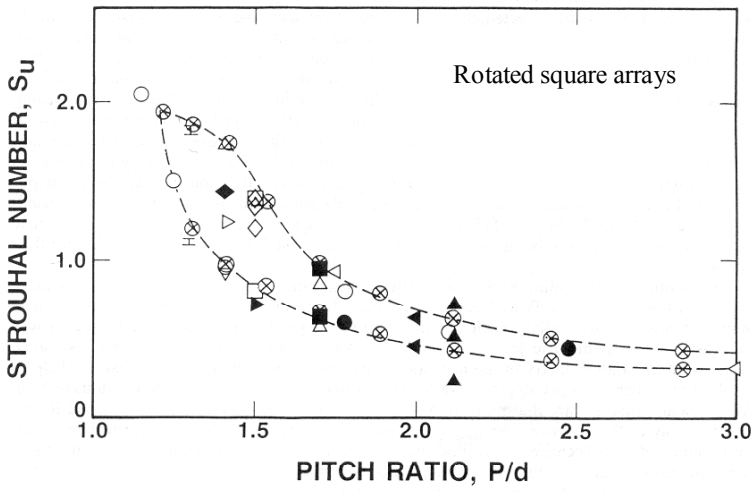

Figure 4.4. Strouhal number chart for rotated square arrays. Note that the Strouhal number is based on the upstream velocity. From Weaver et al. (1993).

5. In-Line Tube Arrays

As in the previous case, the flow characteristics for an in-line array with intermediate tube spacing ratios will be explained first in detail. As shown in Fig. (5.1), the spacing ratios of this array are $X_L = L/d = 1.75$ and $X_T = T/d = 2.25$. Thereafter, the effect of the spacing ratios on the flow mechanisms is discussed.

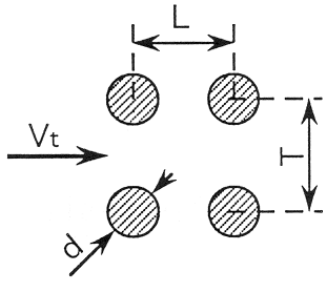

Figure 5.1. Definitions of in-line layout of tube bundles

5.1. In-Line Arrays with Intermediate Tube Spacing

The intermediate spacings array ($X_L/ X_T = 1.75/2.25$) is investigated in air and water flows. Attention is focussed on the first five rows, within which the vorticity shedding excitation is known to reach its maximum level. Here again, extensive correlation measurements are carried out to obtain the amplitude and phase distributions of the fluctuating velocity behind several rows. These distributions are essential to characterize the spatially growing flow instability inside the tube array.

5.1.1. Strouhal number

Figure 1.3 shows typical velocity spectra for air and water flows. The hot wire/film was diagonally centred between the tubes of the second and the third rows. The velocity fluctuations are seen to occur at a well-defined (single) frequency, f_v, which increases as the flow velocity is increased. In the air tests, a higher harmonic component at the frequency, $2f_v$, is also present. The occurrence of this higher harmonic is an inherent feature of separated flows. According to non-linear hydrodynamic stability theory and experimental findings (Ziada & Rockwell,1982), higher harmonics are generated when the amplitude of the fundamental component exceeds about 4% of the mean flow. Since the amplitude of the fundamental component is substantially higher in the air tests (as will be seen later), the harmonic $2f_v$ is well established in the air tests, but not in the water tests. As expected, the Strouhal number of the flow periodicity was found to be the same in air and water flows, and is equal to $S = f_v\, d/V_t = 0.15$, where V_t is the gap velocity, i.e. the same as Vg.

5.1.2. Effect of Reynolds number

The effect of the flow velocity on the root mean square (rms) amplitude of the fluctuating velocity, v, is shown in Fig. (5.2) for the air and the water tests. The hot wire was located behind the second row in the air tests. In the water tests, however, the hot film was moved further downstream, behind the fourth row, to allow measurements of the saturation amplitude which was still not reached behind the second row at the maximum flow velocity. As the flow velocity is increased, the rms amplitude of the fluctuating velocity is seen to increase until it reaches a saturation value of 10 to 12% of the gap velocity. This saturation of v/V_t occurs when the spatially growing flow instability reaches its fully developed phase (e.g. Sato, 1960; Freymuth, 1966; and Miksad, 1972). At relatively high velocities, this saturation value decreases slightly, possibly owing to the increase in the turbulence level. It is important to point out that increasing the flow velocity causes the ratio v/V_t, and not only v, to increase.

Since the ratio v/V_t, at a fixed position, represents the degree of development of the flow instability, the results of Fig. (5.2) indicate that the flow instability behind a certain row becomes more developed as the flow velocity (or the Reynolds number) is increased. This implies that the position at which the flow instability becomes fully developed moves upstream as the Reynolds number is increased.

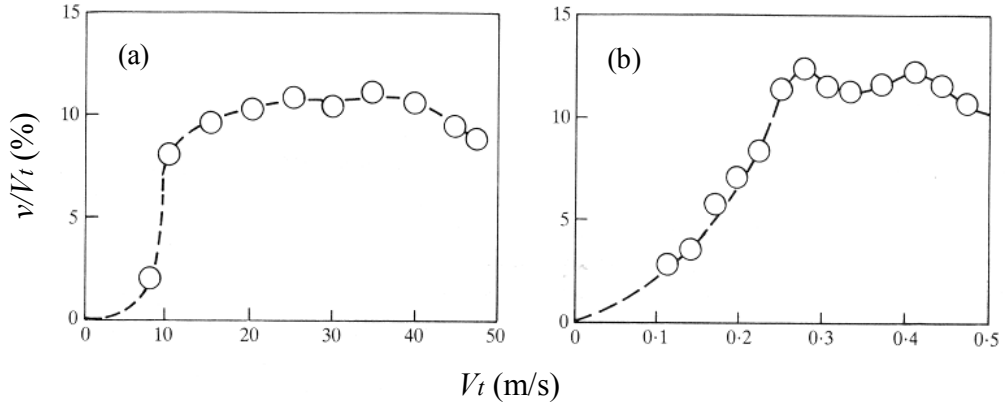

Figure 5.2. Dimensionless amplitude of fluctuating velocity v as function of the gap velocity V_t.
(a) behind row 2 in air tests; (b) behind row 4 in water tests.

5.1.3. Streamwise development of vortivity shedding

The streamwise development of the velocity fluctuation was measured along a line centred between two tube columns of the array tested in water. As shown in Fig. (5.3), the dimensionless amplitude increases in the downstream direction until the fifth row, where it reaches saturation amplitude of about 13%. Behind each row, the fluctuating velocity grows rapidly, but this rapid growth is impeded by the presence of the tubes of the subsequent rows, resulting in the amplitude plateaux at x/L = 1, 2 and 3. These plateaux make the evaluation of the disturbance growth rate within the array rather difficult. Detailed measurements were therefore carried out between the first two rows to gain more insight into the initial stage of the disturbance growth. As shown in Fig. (5.4), the fluctuating velocity grows exponentially in the downstream direction before it is hindered by the tubes of the second row. This exponential growth accords with the prediction of the hydrodynamic stability theory for separated flows, i.e. shear layers, jets and wakes (Michalke 1965; Bajaj & Garg 1977).

The air test facility was used to measure the distributions of the fluctuating velocity amplitude within the development region of the flow instability. The measurements were carried out along the lines centred between the tube rows, and at a flow velocity of 30.6 m/s (Re = 3.8 x 104). Figure (5.5) depicts the distributions across the sixth and the seventh flow lanes (hereafter referred to as

jets). The distributions across the fourth and fifth jets were also measured and were found to be similar to those given in Fig. (5.5). As shown in this Figure, the velocity fluctuation behind the first row are much stronger at the edges of the jet than in its core. This distribution indicates that the flow instability is initiated by the inducement of small velocity perturbations into the shear layers, which separate from the tubes of the first row. These velocity perturbations are amplified exponentially in the downstream direction, as has been shown already in Fig. (5.4). Because the Reynolds number is relatively high, the fluctuation amplitude reaches 13% of the gap velocity already behind the second row. Interestingly, the fluctuation amplitude in the middle of the jet becomes comparable to that at the jet edges. Further downstream, behind the fourth row, the fluctuation amplitude in the middle of the jet becomes substantially higher than that at the jet edges. This gradual change in the shape of the amplitude distributions will be discussed later in conjunction with the phase measurements and the flow visualization study.

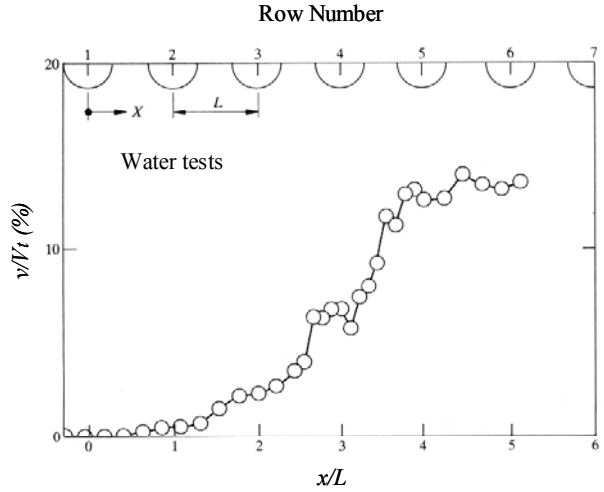

Figure 5.3. Development of the velocity fluctuation along a centreline of a flow lane. Water tests; Re = 6.8×10^3.

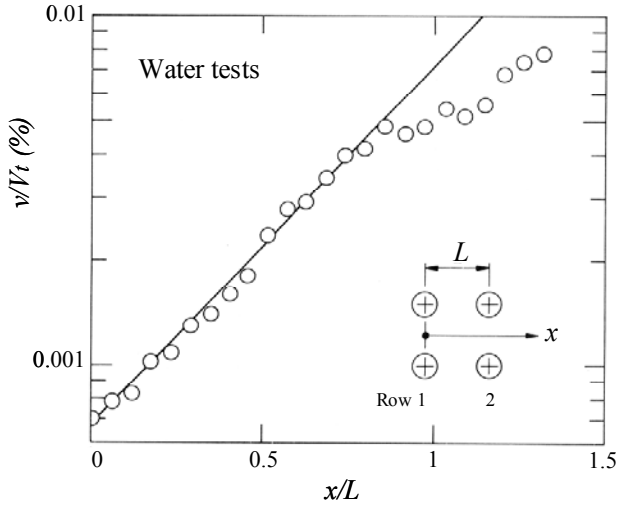

Figure 5.4. Initial exponential growth of the velocity fluctuation. Water tests; Re = 6.8×10^3.

5.1.4. Phase relations

Although the amplitude distributions provide considerable insight into the initial stage and the streamwise evolution of the flow instability, they do not reveal the type or the mode of this instability, neither do they indicate the relationship between the flow oscillations in adjacent jets or wakes. In the following, the phasing of events in adjacent jets is detailed. Since the phase (and coherence) measurements are often somewhat tedious and time-consuming, detailed measurements

were carried out behind the fourth row only. A faster method was then employed, by using two microphones attached to a side wall of the wind tunnel, to show that the phase and coherence distributions behind the other rows are similar to those measured in detail behind the fourth row.

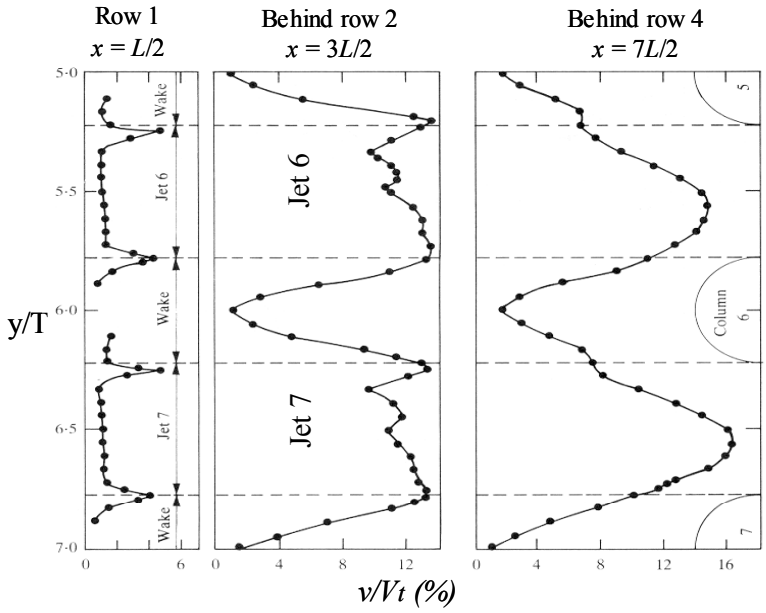

Figure 5.5. Distributions of the dimensionless amplitude of the velocity fluctuation behind the first, the second and the fourth rows. Air tests, Re = 3.8×10^4.

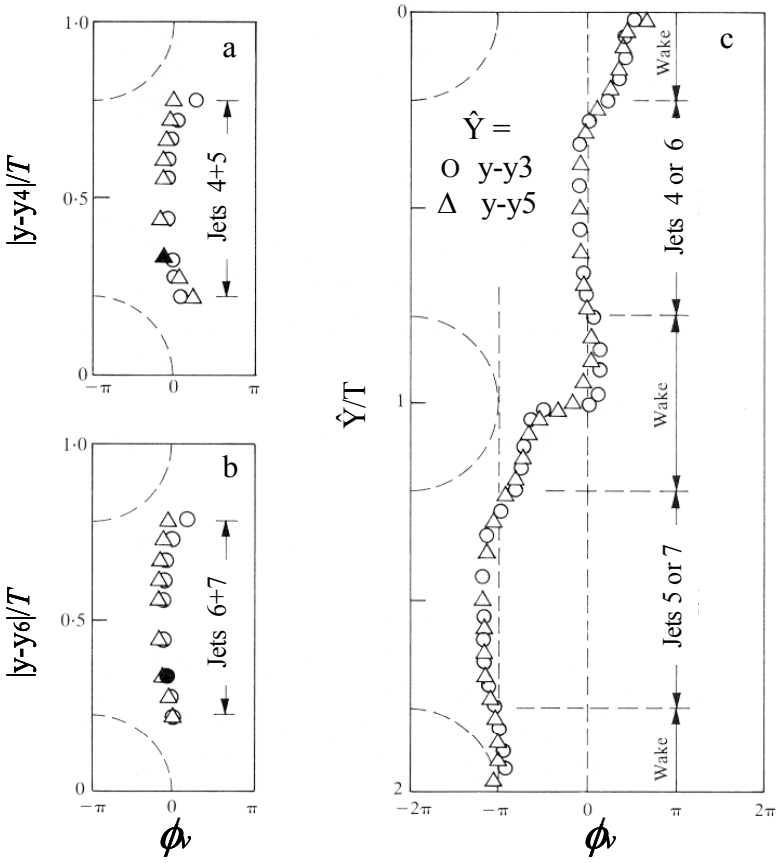

Figure 5.6. Phase distributions of the velocity fluctuation behind the fourth row at *x = 7L/2.* Air tests, Re = 3.8×10^4. (a) ○, ϕ_{v4}; Δ, $\phi_{v5} + \pi$; (b) ○, ϕ_{v6}; Δ, $\phi_{v7} + \pi$; (c) ○, ϕ_{v4} and ϕ_{v5} ; Δ, ϕ_{v6} and ϕ_{v7} ; ●, ▲, reference locations.

The phase distribution of the velocity fluctuation behind the fourth row is given in Fig. (5.6). The round data points in insets a & b represent the phase variations across jets 4 and 6, respectively. The triangular data points correspond to the phase across jets 5 and 7, but after adding a value of π. The phase distribution across anyone jet is seen to be *symmetric*, i.e. the velocity fluctuations occurring at one edge of a jet is in phase with that at the other edge. Moreover, the velocity fluctuation in any jet as a whole is 180° out of phase with that in the neighbouring jet. The phase distributions across the four jets 4 to 7 are presented together in Fig. (5.6.c). This figure emphasizes the remarkably organized nature of the flow activities. Jet 5, for example, is in phase with jet 7, but is 180° out of phase with the neighbouring jets (jets 4 and 6). Additional measurements behind other rows yielded similar results.

5.1.5. Global structure of vorticity shedding excitation

Flow visualization pictures taken at different locations within the array, but at the same time instant of the cycle, were pieced together to construct the development of the flow structure within the first five rows. The signal of the hot film, which was kept in a fixed location, was used as a time reference. The result of this piece-wise method of flow visualization is shown in Fig. (5.7). The flow structure in the flow lane, Fig. (a), displays, very clearly, a symmetric mode of an unstable jet. The symmetry with respect to the jet centreline and the clarity of the jet structure are rather remarkable. In the tube wakes, Fig. (b), the vortices form in an anti-symmetric pattern. Moreover, the vortex pattern in each wake is nearly out of phase with these in the upstream and downstream wakes. It should be mentioned here that this anti-symmetric pattern in the tube wakes is phenomenologically different from the alternating vortex shedding in the wakes of isolated cylinders.

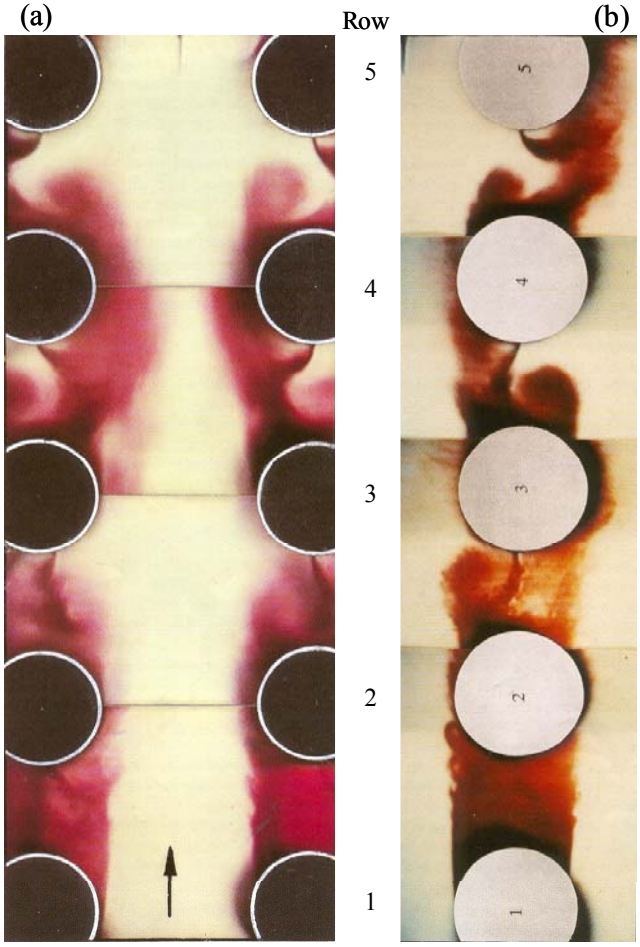

Figure 5.7. Flow visualization photographs showing the global flow structure in (a) a flow lane and (b) several tube wakes. Re = 1.5×10^4.

5.1.6. Description of the flow instability in in-line arrays

When the tubes are arranged in an in-line pattern, they form free-flow lanes and confined tube wakes. As the flow proceeds into the array, a jet-like profile develops continuously along the flow lanes, but a wake profile never develops in the tube wakes. Thus, the flow dynamics in the flow lanes would be expected to dominate the development of the velocity fluctuations within the array. Accordingly, the vorticity-shedding excitation is caused by the instability of the jets which proceed along the flow lanes.

The jet instability is initiated at the locations of flow separation from the tubes in the first row. In this initial region, the velocity fluctuation is still small and is manifested primarily in the thin shear layers of the jet. Between the first and the second rows, the velocity fluctuation undergoes a spatial exponential growth, which is in accordance with the linear theory of hydrodynamic stability. Furthermore, the amplitude and the phase of the initial velocity fluctuation have symmetric distributions with respect to the jet centreline. These initial distributions dictate the symmetric pattern of the jet instability developing downstream. The interaction of the developed jet with the downstream tubes is fed back upstream, where new perturbations are induced at the initial region near separation.

As the flow proceeds downstream, or as the Reynolds number is increased, the amplitude of the velocity fluctuation grows until it reaches the non-linear saturation amplitude, typically about 15% of the gap-flow velocity. Further downstream, the increase in the turbulence level reduces the saturation amplitude slightly. The jet instability occurs at a preferred symmetric mode. Large-scale vortices are formed symmetrically at both sides of each flow lane. Because of the kinematic constraints imposed by the large size of the formed vortices and the associated mass transfer across the wakes, vortices are forced to form anti-symmetrically in the tube wakes. This dictates the phase difference between the flow activities in adjacent flow lanes. Thus, the jet instability occurring in each flow lane is 180° out of phase with that occurring in the neighbouring lanes.

5.2. Simulation of Resonance by Means of Surface Waves in Water Channel

The acoustic resonance occurring in the wind tunnel can be simulated by a transverse surface-wave resonance in the water channel. During the water tests on the intermediated spacing case, the first mode of the transverse standing waves was excited. This mode consisted of a half wavelength spanning the width of the channel as shown in Fig. (2.2). Since the tubes were mounted vertically in the channel, the particle velocity of the surface wave, away from the sidewalls, had a predominant component in a direction normal to the flow and the tube axes. Moreover, the standing wave was found to be confined to the tube bundle; its amplitude being maximum at the mid-depth of the array and decreasing in the upstream and downstream directions. These features are similar to those of the acoustical modes in the wind tunnel.

5.2.1. Resonant flow structure

The flow structure in the array from the first to the fifth rows under resonance conditions is given in Fig. (5.8). Each photo in this figure has been taken at the same instant of time within the oscillation cycle. The photos, therefore, display the global view of the resonant flow structure within the array. As illustrated, the vortices behind all tubes have the same sense and phase. This synchronization is clearly caused by the surface wave resonance. The size and the swing angle of each vortex are related to the resonance intensity at the vortex location. Near the first and last rows the vortex size and swing angle are smaller than those at the middle row where the surface wave resonance is strongest.

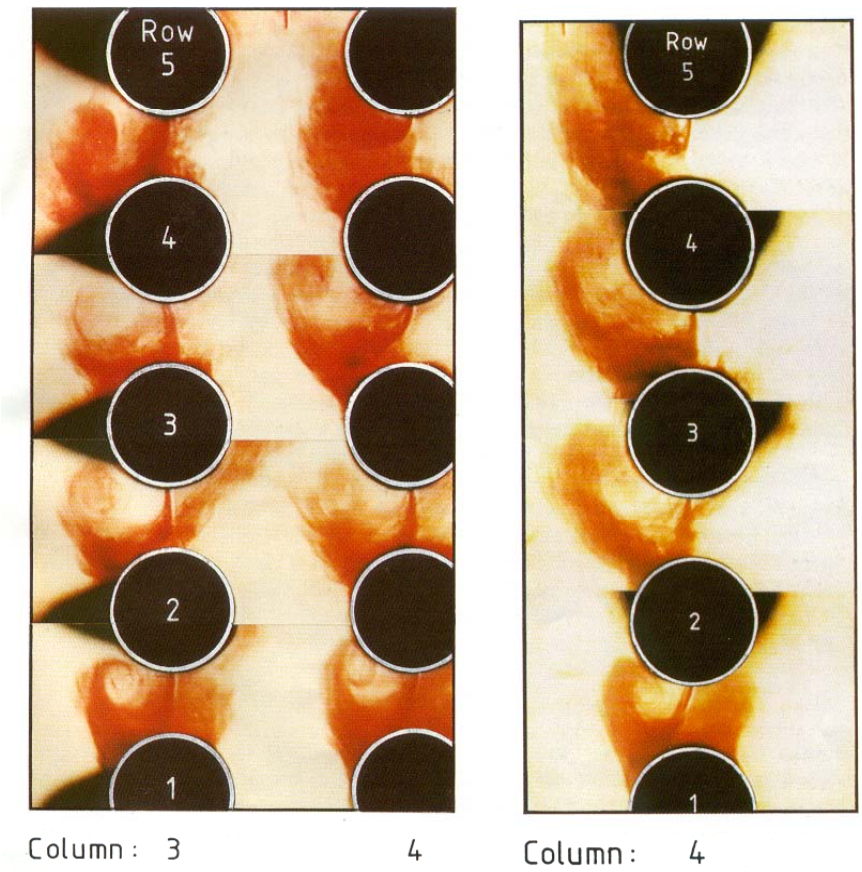

Figure 5.8. Overview of the resonant flow structure in the array at the same instant of time in a period of surface wave resonance.

It would be misleading to relate the observed resonant flow structure to wake instability such as that which creates Karman vortices in the wakes of isolated cylinders. The tube wakes in the present case are confined, owing to the presence of the downstream tubes. The streamwise gap between the tubes, i.e. the extent of the tube wakes, is less than the tube diameter. A wake velocity profile does not develop in such a confined wake. Thus, the tube wakes can be regarded as cavities bounded by the shear layers, which separate from the tube edges. It is the instability of these shear layers, triggered and synchronized by the resonance mode, which generates the observed resonant flow structure.

5.2.2. Resonance mechanism

The resonant flow structure, Fig. (5.8), and the non-resonant flow structure associated with the vorticity-shedding excitation in the absence of resonance, Fig (5.7) are compared schematically in Fig. (5.9). It is clear that the resonant structure can couple with a fluid resonance, which induces a particle velocity in the transverse direction as shown by the arrows in Fig. (5.9.a). The vorticity-shedding excitation, however, cannot couple with such a resonance. As shown in Fig. (5.9.b) , the vortex pattern confined to a tube column is 180° out of phase with those confined to the neighbouring columns. The resultant-flow excitation produced by this vortex pattern in the transverse direction is, therefore, practically zero.

The above argument can be substantiated further by considering the acoustic power, W, generated by an array of vortices in an acoustic field. Howe (1975, 1980) showed that the acoustic power generated in a volume $\mathcal{V}$ can be expressed by:

$$W = -\rho \int \boldsymbol{\omega} \,.\, (\boldsymbol{V} \times \boldsymbol{u}) \; d\mathcal{V} \qquad (4)$$

where, ρ is the density, $\boldsymbol{\omega}$ is the vorticity, $\boldsymbol{V}$ is the total flow velocity and $\boldsymbol{u}$ is the acoustic particle velocity. Since all the vortices in Fig. (5.9.a) have the same sense of rotation, their effect on the above integral will be cumulative, resulting in a net acoustic power which sustains the resonance. In Fig. (5.9.b), however, the vorticity vector of half of the vortices is opposite to that of the other half. This means that half of the vortices will be acoustic sources and the other half will be acoustic sinks. The net effect of the above integral will be insignificant.

It should be emphasised that each of the flow patterns given in Fig. (5.9) satisfies well defined, but different phase relations. These patterns therefore are associated with different flow instabilities. Pattern (b) is the result of symmetrical jet instability, which is the preferred mode of oscillation at non-resonant conditions. However, pattern (a) results from shear-layer instability, which is triggered and synchronized by the resonant particle velocity. Since the shear-layer mode is suppressed at off-resonant conditions, because it is not a preferred mode, the occurrence of resonance is dependent on the capability of the flow-duct acoustics to initiate and sustain this shear-layer mode.

Since the flow instabilities causing the resonance and the vorticity-shedding excitation are different, it is logical to expect them to occur at different Strouhal numbers. This is compatible with the experimental observation that the acoustic resonance Strouhal numbers are different from the Strouhal number of vorticity shedding. These findings give support to the supposition that Strouhal numbers of vorticity shedding should not be determined from resonance cases.

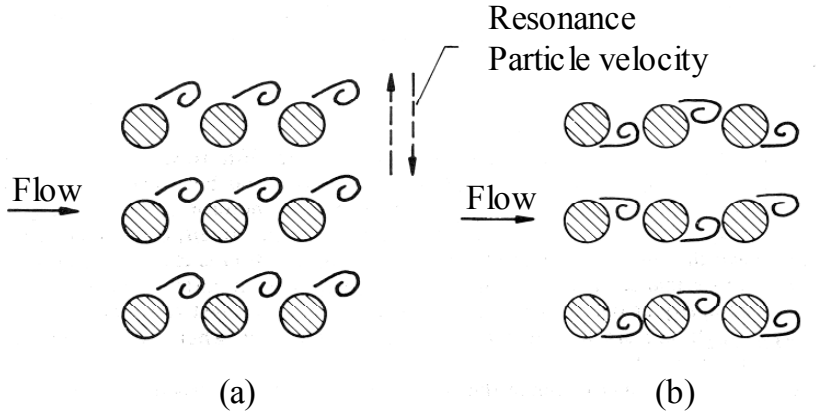

Figure 5.9. Schematics illustrating (a) the resonant and (b) non-resonant vortex shedding patterns.

5.3. In-Line Arrays with Small Tube Spacing

When the tube spacing ratios are reduced, the vortices resulting from the symmetric jet instability do not form entirely inside the tube wakes as in the previous case, but rather in the thin shear layers at both sides of the flow lanes. An example is shown in Fig. (5.10) for which the spacing ratios are $X_L = 1.4$ and $X_T = 1.5$. In this case, the vortices have a very small size, especially in comparison with the width of the wake, i.e. the tube diameter. The resulting mass transfer across the wakes, due to these small size vortices, is therefore negligible. This allows the wake vortices to form symmetrically, and therefore adjacent flow lanes oscillate in phase with one another.

For small spacing ratios, the vorticity shedding excitation is found to occur within the upstream rows only. Downstream of the third row, these small size vortices diffuse rapidly into small-scale turbulence and the flow becomes fully turbulent. This is in contrast with the case of intermediate tube spacings for which the vorticity shedding excitation (i.e. the symmetric jet instability) persists

over the whole depth of the bundle. More details of the flow structure for the case of small spacing ratios can be found in Ziada et al. (1989).

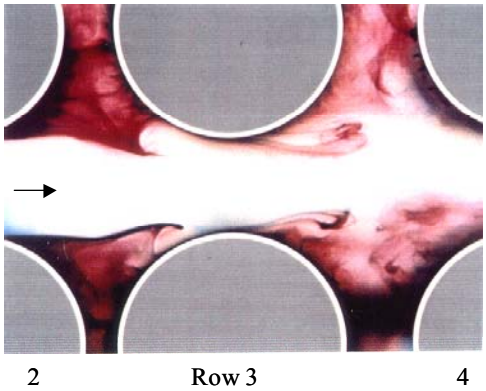

Figure 5.10. Flow structure in an in-line bundle with small spacing ratios. X_L = 1.4, X_T = 1.5, Re = 3.7 x 10^3, flow direction is from left to right.

5.4. In-Line Arrays with Large Tube Spacing

For large spacing ratios, the nature of the vorticity shedding excitation and its Strouhal number depend on the upstream turbulence level, Tu, which was controlled by adding a turbulence-generating grid upstream of the bundle. At low upstream turbulence levels (T_u ~ 0.1 %), the vorticity shedding is identical to that observed for intermediate spacing ratios. This fact is shown in Fig. (5.11) which depicts the symmetric jet instability for spacing ratios of X_L / X_T = 3.25/3.75. The velocity fluctuations in neighbouring flow lanes (or wakes) are found to be strongly correlated and 180° phase shifted from one another. As in the case of intermediate tube spacings, this vorticity shedding mode dominates over the whole depth of the bundle.

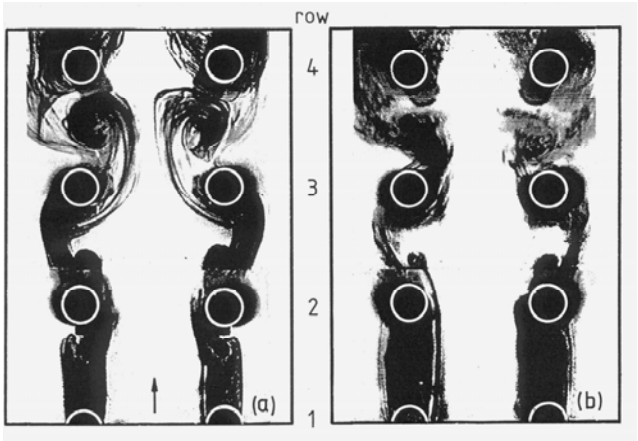

Figure 5.11. Symmetric jet instability producing the first mode of vorticity shedding inside a tube bundle with large spacing ratios. (a) Re = 800, (b) Re = 2.6 x 10^3, both cases without turbulence-generating grid. X_L = 3.25; X_T = 3.75.

The second mode of vorticity shedding occurs when the turbulence level is increased (Tu ~ 1.0%). This mode has a higher Strouhal number and dominates at the upstream rows only. It is found to be generated by local instabilities of the tube wakes. This is demonstrated by the photos given in Fig. (5.12), which were taken at the same flow conditions. In Photo (a), vortex shedding in adjacent wakes is out of phase but in Photo (b), it is in phase. This lack of correlation between the flow activities in adjacent wakes was also confirmed by means of phase and coherence measurements. Further details of the flow structure inside bundles with large spacing ratios can be found in Oengoeren & Ziada (1993).

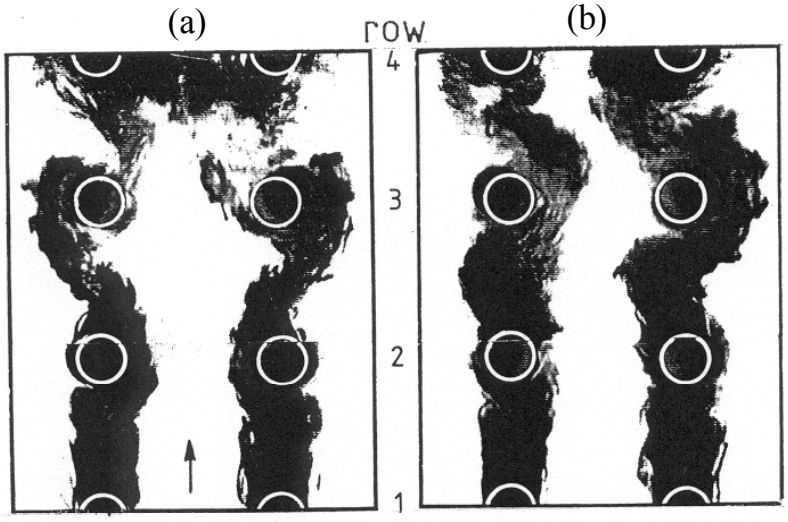

Figure 5.12. Second mode of vorticity shedding in a tube bundle with large spacing ratios and high upstream turbulence level. Both photos were taken at the same flow velocity ($Re = 2.6x10^3$) and with a turbulence grid installed upstream of the bundle. $X_L = 3.25$; $X_T = 3.75$.

5.5. Strouhal Number Charts for In-Line Arrays

5.5.1. Strouhal number of vorticity shedding (S_v)

The Strouhal number of vorticity shedding is defined by:

$$S_v = f_v\, d \,/\, V_t \tag{5}$$

where, f_v is the frequency of the vorticity shedding peak in the turbulence spectra and V_t is the gap velocity. Figure (5.13) gives the value of S_v as a function of the tube spacings (X_L and X_T). In order to reduce the data scatter and therefore improves the reliability of the data, the following approach was adopted to construct the Strouhal number chart:

(i) All the data obtained from tube or acoustic resonances were rejected.
(ii) The data used to construct the chart were all obtained from measurements at high Reynolds number ($Re > 10^4$).
(iii) Hot wire/film measurements are considered to be more reliable than other measurements (e.g. tube vibrations).
(iv) Higher harmonics of the vorticity shedding excitation (i.e. $2\,f_v$, $3\,f_v$, ...) were not taken into consideration.
(v) In few cases, several peaks in close proximity to one another were observed (e.g. 0.12, 0.14, 0.16). An average value was considered representative in these cases (0.14).

Figure (5.13) can be used to determine the critical flow velocity ($V_{cr} = f_n\, d \,/\, S_v$) at which a tube resonance may occur, where f_n is the tube mechanical resonance frequency. If this critical velocity is found to be within the operating range, the vibration amplitude should be calculated to check whether lock- in vibration will or will not occur.

5.5.2. Strouhal number of acoustic resonance (S_a)

As mentioned earlier, acoustic resonances of in-line tube bundles are excited by the unstable shear layers which separate from the tubes. Since this mechanism is different from the vorticity shedding mechanism, the Strouhal numbers of acoustic resonances (S_a) must be different from the

vorticity shedding Strouhal numbers. Therefore, any reliable design guidelines must include two Strouhal number charts; one for vorticity shedding excitation, Fig. (5.13), and another for acoustic resonance excitation.

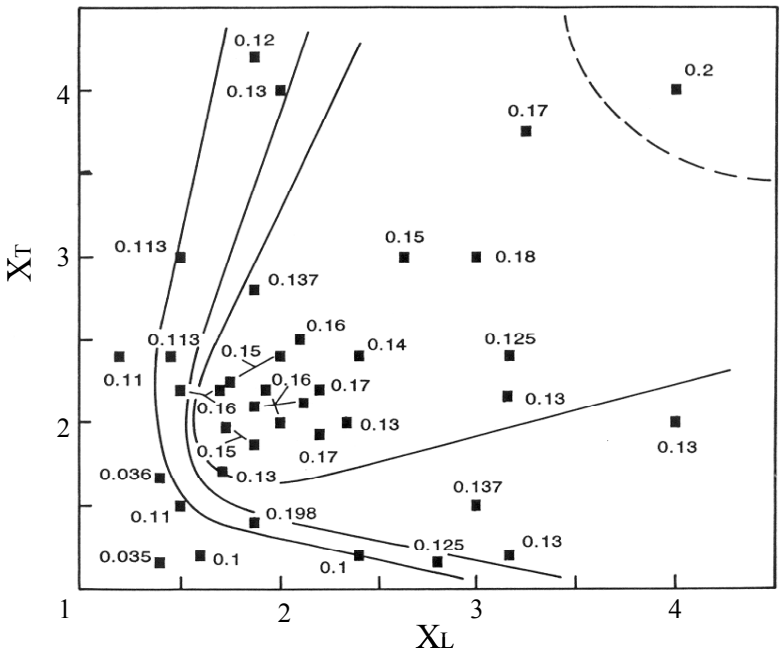

Figure 5.13. Strouhal number chart for vorticity shedding excitation in in-line arrays, $S_v = f_v\, d \,/\, V_t$

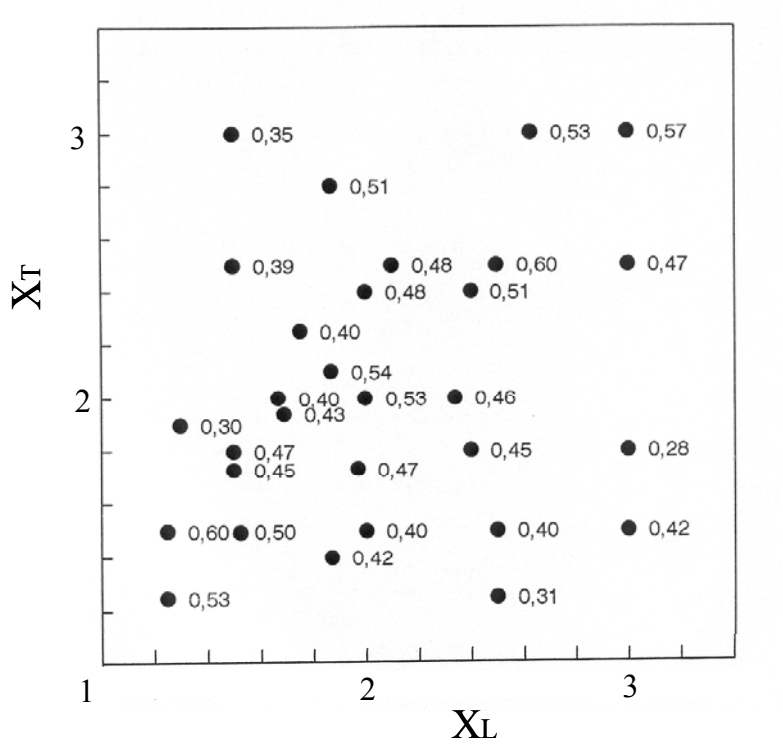

Figure 5.14. Strouhal number chart for acoustic resonance in in-line arrays, $S_a = f_a\, L \,/\, V_t$

The Strouhal number at which acoustic resonances occur is given in Fig. (5.14). This Strouhal number is based on the streamwise tube spacing L and the frequency of the acoustic mode f_a.

$$S_a = f_a \, L / V_t \tag{6}$$

The usage of L as the characteristic length results in a nearly constant S_a over a wide range of X_L and X_T. This nearly constant value is about 0.5, which is similar to the Strouhal number at which acoustic resonances in deep cavities occur. Since the excitation mechanisms of the two cases are somewhat similar, it is logical that the Strouhal numbers are also similar. For large spacing ratios (X_L, $X_T > 3.0$), acoustic resonances are excited by the vorticity shedding excitation, and therefore the vorticity shedding Strouhal number, Fig. (5.13), can be used to design against acoustic resonances. The critical flow velocity at which *acoustic resonances* may occur can be obtained from: $V_{cr} = f_a \, L / S_a$. If V_{cr} is found to be less than the maximum flow velocity, the acoustic resonance frequency f_a should be increased by installing antiresonance baffle plates.

5.6 Summary of Results for In-Line Tube Bundles

Basically, there are three different types of flow instabilities, which can generate periodic flow excitations in in-line tube bundles, these being: symmetric jet instability; wake instability and shear-layer instability. In the following, in-Iine tube bundles are classified according to the flow instability which dominates in each class.

5.6.1. Large tube spacings ($X_L > 2.7$)

Vorticity shedding in in-line tube bundles with large spacing ratios can occur at either a global jet mode or a local wake mode. These two modes have different Strouhal numbers and do not occur simultaneously. The occurrence of either mode depends primarily on the turbulence level in the approach flow.

At low upstream turbulence level, the symmetric instability of the jets issuing between the tube columns dominates. This mode of vorticity shedding persists over the whole depth of the bundle and is identical to that occurring inside in-line tube bundles with intermediate spacing ratios. The flow activities in adjacent wakes or flow lanes are found to be well correlated and to satisfy well-defined phase relations. Due to these features, this first mode may be regarded as a "global" flow instability.

When the upstream turbulence level is high, the vorticity shedding switches to a "local" wake instability mode. Alternating vortex shedding in each wake becomes more or less independent from those in adjacent wakes. This mode occurs only at the upstream rows. Downstream of the fifth row, it is totally replaced by a broadband turbulent excitation at a different frequency. The wake instability mode of vorticity shedding is capable of exciting acoustic modes, when its frequency approaches a resonance frequency. At resonance, i.e. at lock-in, vortices in all wakes are synchronized with the particle velocity of the resonant mode. As in the case of intermediate tube spacings, the jet instability mode of the vorticity-shedding excitation cannot excite the acoustic modes which consists of standing waves in the transverse direction. During the water tests, the occurrence of free surface resonance was associated with flow switching from the jet mode to the wake instability mode.

Since the upstream turbulence level in practical applications is relatively high, the wake instability mode of the vorticity-shedding excitation is expected to dominate in tube bundles with large spacings. This may not be the case for bundles with intermediate spacing ratios, for which the jet instability mode occurs also at relatively high upstream turbulence level.

5.6.2. Intermediate tube spacings ($1.75 < X_L < 2.7$)

Vorticity shedding in tube bundles with intermediate tube spacings is generated by a global jet mode and it persists over the whole depth of the bundle. The occurrence of acoustic resonance in this case is caused by the coupling between the resonant acoustic mode and the instability of the shear layers which separate from the tubes. This shear layer mode, however, does not occur, i.e. it is suppressed, at off-resonance conditions.

5.6.3. Small tube spacings ($X_L < 1.5$)

When the tube spacings are made smaller, the jet instability becomes weaker and, if it materializes at all, it occurs at the upstream rows only. As in the previous case, acoustic resonances in this case also are excited by the shear layer instability.

6. Parallel Triangle Tube Arrays

Since parallel triangle tube bundles have a staggered pattern of tube layout, Fig. (6.1), they have been treated in early literature under the general category of staggered tube arrays. However, as illustrated in Fig. (1.1) parallel triangle arrays allow the flow to proceed along the free lanes between adjacent columns, which is rather similar to the in-line case. As a result of these combined geometrical constraints, i.e. *free flow lanes through staggered array* of tubes, the mechanisms of flow instabilities are expected to be more complex in parallel triangle arrays. As in previous cases, the flow characteristics will be discussed for each category of tube spacing separately.

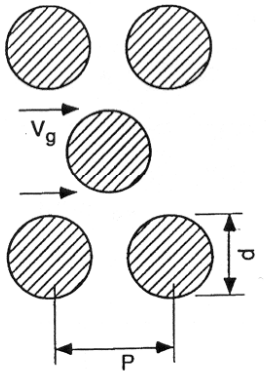

Figure 6.1. Definitions of parallel Triangle layout of tube bundles

6.1. Parallel Triangle Arrays with Intermediate Tube Spacing

A parallel triangle array with X_p = 2.08 is selected to elucidate the flow mechanisms in intermediate spacing arrays. For this array, pressure spectra measured at a front (row 1) and a rear row (row 5) are displayed for different Reynolds numbers in Fig. (6.2). Although the dominance of a single frequency component is observed in the spectra of both rows, these components have different Strouhal numbers and therefore they belong to different flow periodicities occurring at these rows. The component detected at row 1 has a Strouhal number of $S_2 = f_{v2}\, d/V_g = 0.48$, whereas the one measured at row 5 corresponds to $S_1 = f_{v1}\, d/V_g = 0.28$. Both of these components exist simultaneously in the array regardless of the Reynolds number indicating that a transition takes place from the periodic structure S_1 to S_2 as the flow proceeds downstream in the array. The component S_1 (or f_{v1}) is enhanced at higher Reynolds numbers, and is an order of magnitude higher than S_2 at Re = 18000. It is noteworthy that at Re = 18000, an enhancement of the first acoustic mode f_{a1} is observed in both spectra, indicating the onset of acoustic resonance although the component f_{v1} is still significantly lower than the resonance frequency, f_{a1}, and the f_{v2} component has already passed this frequency without inducing resonance.

The same tube array geometry (X_p = 2.08) was also tested in water. Two photos displaying the flow patterns behind the first two rows at a Reynolds number of Re=1870 are shown in Fig. (6.3). The Strouhal number corresponding to the well-defined vortices observed in this figure are determined to be 0.46 from the video counting. This Strouhal number is very close to S_2, which is measured at the first row in air tests. As observed in Fig. (6.3), vortex shedding behind the first row can occur at two patters, either symmetric or antisymmetric. The change from one mode to the other occurs randomly but the vortices of both modes are shed at the same frequency.

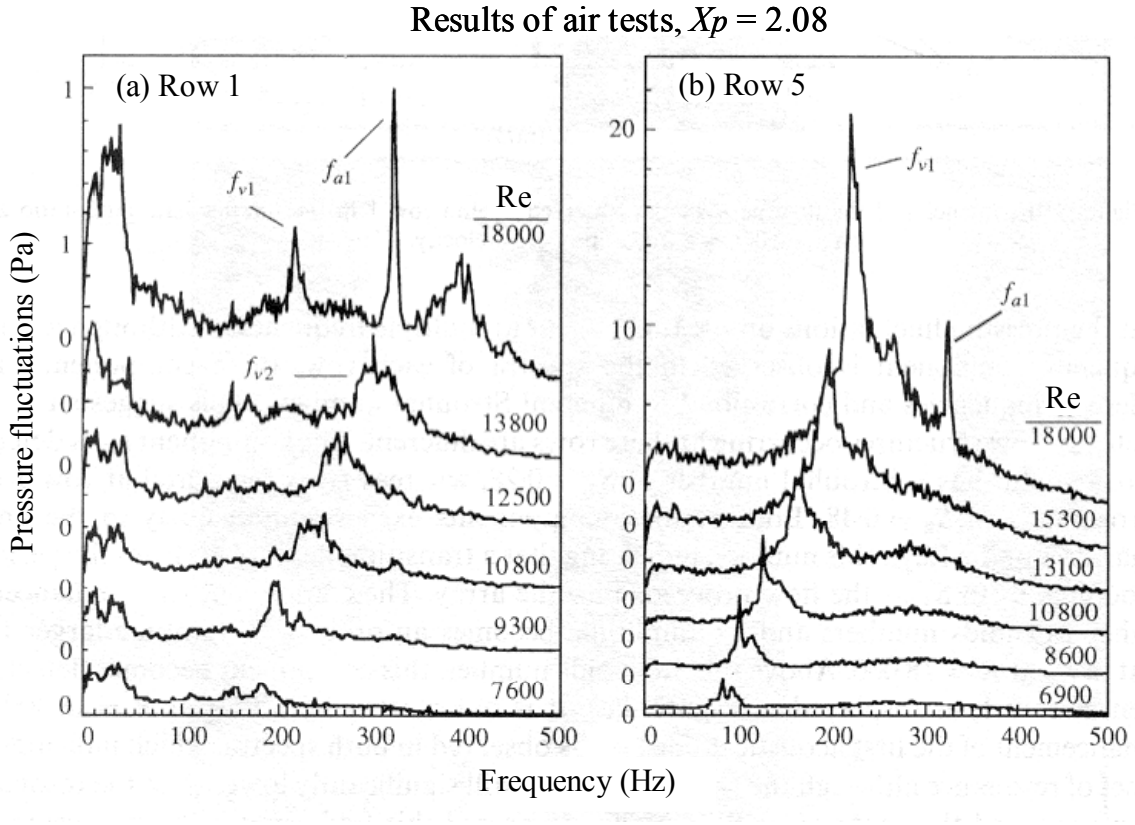

Figure 6.2. Pressure spectra measured at (a) row 1 and (b) row 5 in a *parallel triangle array with intermediate spacing*, X_p = 2.08, and for a Reynolds number range of 6900< *Re* < 18000.

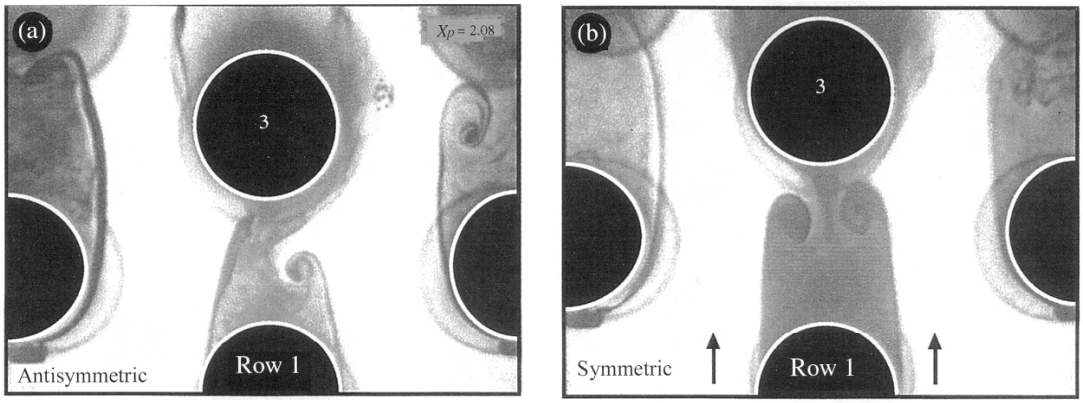

(a) Antisymmetric (b) Symmetric

Figure 6.3. Flow visualization photographs showing the flow patterns associated with the flow periodicity S_2. *Parallel triangle array with intermediate spacing*, X_p = 2.08, and for a Reynolds number of 1870.

The photos of the flow pattern occurring in the same array at a relatively high Reynolds number (Re = 12300) are given in Fig. (6.4). These photos were taken at the same time instant of the vortex shedding cycle and therefore they represents the global flow structure developing in the array at this Reynolds number. In Fig. (6.4), minimal flow unsteadiness is observed behind the first two rows. The dye boundary marking the shear layers separating from the first row tubes is reattached to the

tubes in the third row and does not exhibit lateral oscillations. There is considerable shear layer oscillations behind rows 3 and 4, however, coherent vortices do not form in this region as can be seen in the photos of these rows. Coherent vortices first appear behind the fifth row. The formed vortices are as large as the tube pitch and are shed at a Strouhal number of ≈ 0.24, as counted from the video monitor. This value is close to S_1 of the air tests suggesting that they represent the same flow periodicity.

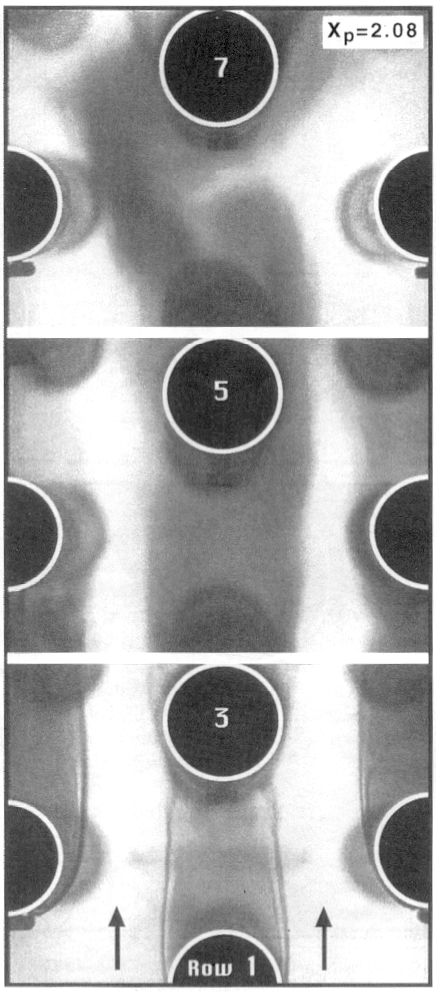

Figure 6.4. Development of the flow structure associated with the flow periodicity S_1. *Parallel triangle array with intermediate spacing*, X_p =2.08, and for a Reynolds number of 12300.

6.2. Parallel Triangle Arrays with Small Tube Spacing

A tube array with X_p = 1.44 is discussed here in detail as a representative example of parallel triangle arrays with small pitch ratios. In Fig. (6.5), a series of pressure spectra measured at the fifth row in this array is shown for a Reynolds number range of 940 to 6590. As seen in this figure, similar to the intermediate spacing array, the flow has a multiple frequency nature over a relatively large Reynolds number range. However, the peaks appearing in Fig. (6.5) are found to be associated with different flow structures and, therefore, they are designated as f_{v3} and f_{v4}, instead of f_{v1} and f_{v2} as in the intermediate spacing case. This designation is made because the Strouhal numbers corresponding to the former peaks are much higher than those of the latter.

As seen in Fig. (6.5), the flow activities appear first as a single frequency event, f_{v3}, at very low Reynolds numbers, Re < 1000. As the Reynolds number is increased over 1000, a second

component, f_{v4}, appears in addition to f_{v3} in the pressure spectra. This component is much sharper and stronger than f_{v3}. It gains in strength within the range $1400 < Re < 3290$, and subsides abruptly when Re is increased over this range. These characteristics suggest that this component is caused by a *local* periodic flow phenomenon, which appears to move (upstream) along the depth of the bundle as the flow velocity is increased. On the other hand, the f_{v3} component survives in a larger range of Reynolds numbers, $0 < Re < 5165$. However, following some enhancement at the lower values of this range, it gradually turns into a broad-banded event and then ceases to exist when Re is increased over 5165. The pressure spectrum measured at row five for Re = 6590 displays the characteristics of a turbulent flow.

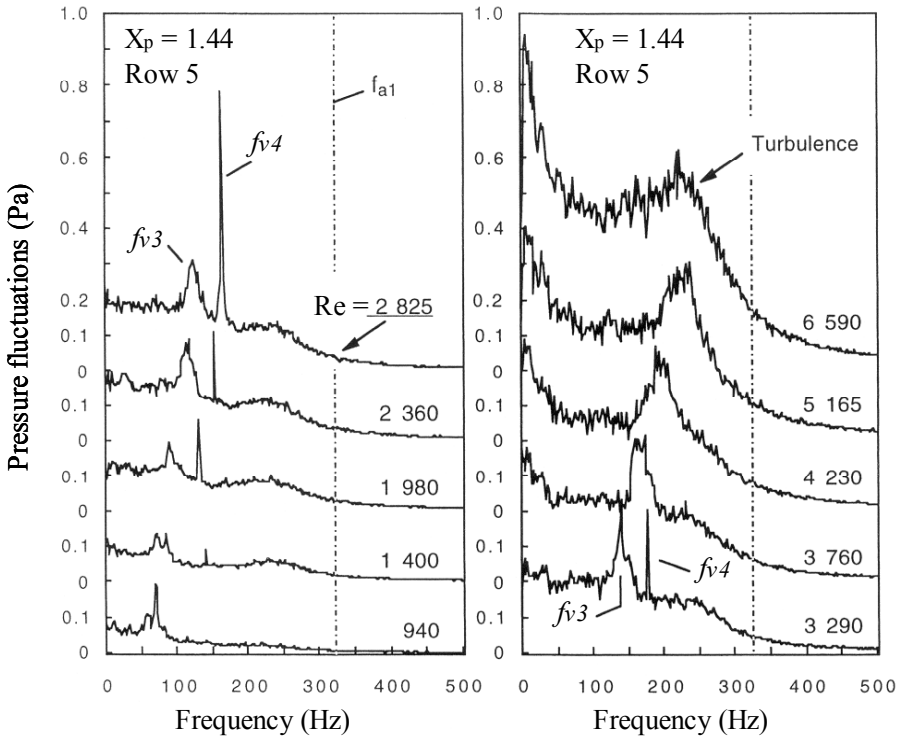

Figure 6.5. Typical pressure spectra obtained at different Reynolds numbers at the fifth row of a parallel triangle array with small spacing ratio, X_p = 1.44.

In order to clarify whether or not the periodic events disappear throughout the whole bundle, the pressure spectra measured at the first two rows are shown in Fig. (6.6) in comparison to that of row 5 for a Reynolds number of 17000. The frequency components, f_{v3} and f_{v4}, do not exist in any of the three spectra obtained at rows l, 2 and 5 as seen in this figure; all three spectra display the characteristics of a fully turbulent flow. The peak appearing in the spectra of rows 1 and 2 around a frequency of 324 belongs to the first acoustic cross mode of the test-section, f_{a1}.

The flow periodicities, f_{v3} and f_{v4}, are further investigated in the water channel with a tube bundle model having the same array geometry as the one described above which was tested in air. Figure (6.7) shows the flow pattern visualised in a flow lane from the first to the eleventh row at a Reynolds number of 580. The flow proceeds mainly in the free lane between the two tube columns displayed in this figure. The shear layers developing on both sides of the flow lane are clearly traced by the streak lines on each side. The amount of unsteady flow activities is minimal behind rows 1 to 4; no unsteady motion could be seen on the video screen at this portion of the flow lane in this case. The flow becomes gradually more active as it moves deeper inside the bundle. In fact, some rotational motion of the flow is apparent in the shear layers on both sides of the flow lane behind the fifth row. These activities develop into well-defined vortices behind rows 7 and 8 as observed in Fig. (6.7). The nature of this flow unsteadiness is displayed in the two hot-film spectra

given at the bottom of Fig. (6.7). Both spectra contain clear peaks, although visually little unsteady activity is observed behind row 1. The peaks have the same frequency, but the amplitude of the peak measured behind row 1 is an order of magnitude weaker than that measured behind row 5. These features, in addition to the flow visualisation, illustrate the developing nature of flow periodicity from front to the rear rows at low Reynolds number. The frequency of this flow periodicity corresponds to the component f_{v3} observed in the results of the air tests already addressed in Fig. (6.5).

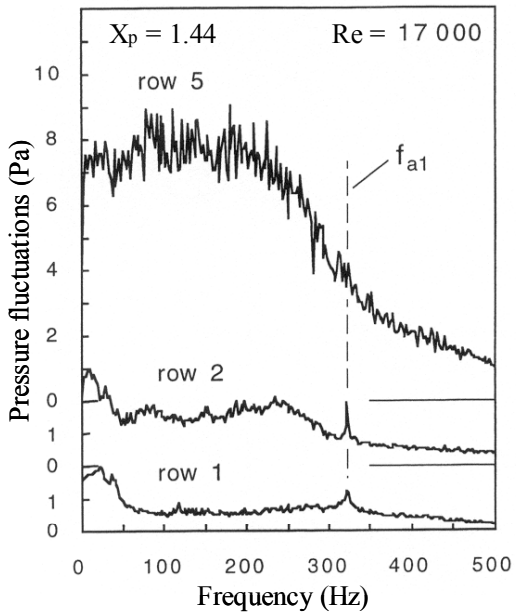

Figure 6.6. Typical pressure spectra measured at rows l, 2 and 5 at a Reynolds number of Re=17000 in a parallel triangle array with small spacing, X_p = 1.44.

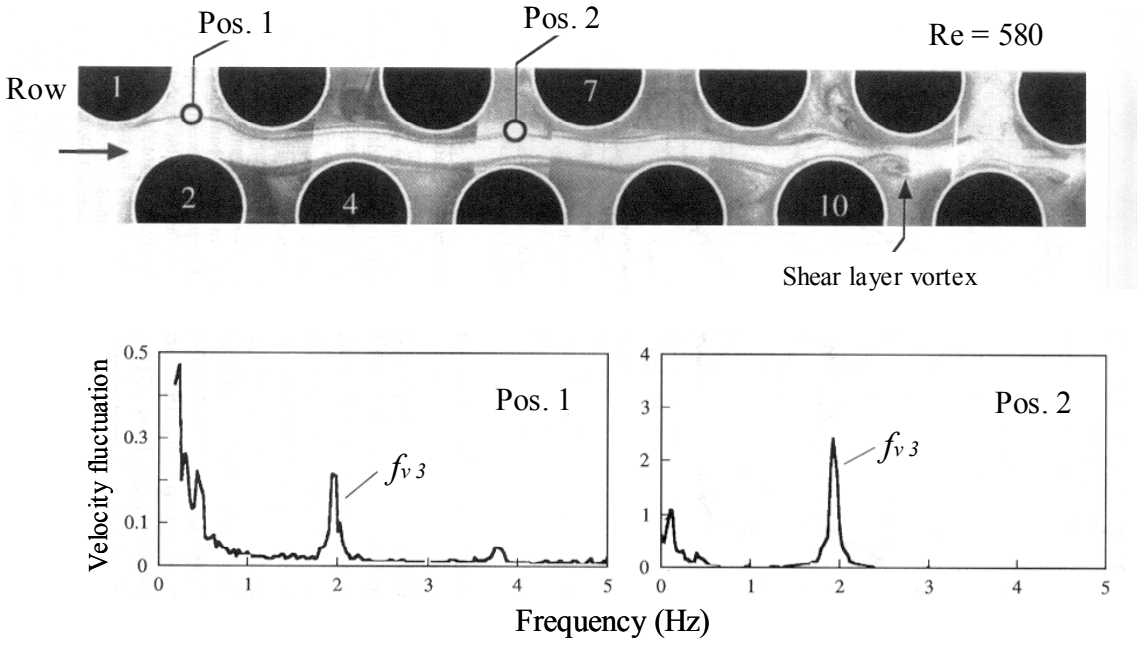

Figure 6.7. Flow patterns observed in a flow lane of a parallel triangle array with a small spacing, X_p = 1.44, at a Reynolds number of 580 and corresponding hot film spectra measured in water flow behind rows 1 and 5.

6.3. Parallel Triangle Arrays with Large Tube Spacing

Figure (6.8) shows three spectra of the fluctuation pressure measured on a tube in the first row of a parallel triangle array with large spacing, X_p = 3.41. Because these tests were carried out in the wind tunnel, the Reynolds numbers corresponding to these spectra are relatively high; 15000, 30000 and 43700, respectively. Each of these spectra displays only one flow periodicity peak corresponding to a Strouhal number of S = 0.22. Pressure measurements at other rows revealed this peak at S = 0.22 to be the only periodic component existing in the whole array regardless of the measurement location. It persists and preserves its narrow-banded character deep inside the array.

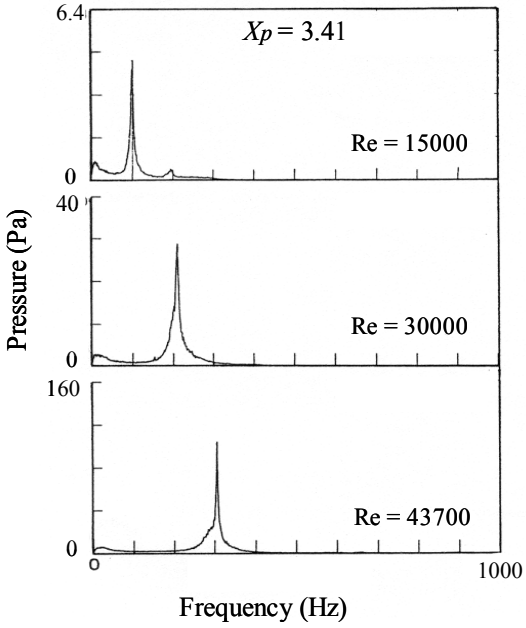

Figure 6.8. Pressure spectra showing the flow periodicity S_1 at the first row of a large spacing parallel triangle array, X_p = 3.41.

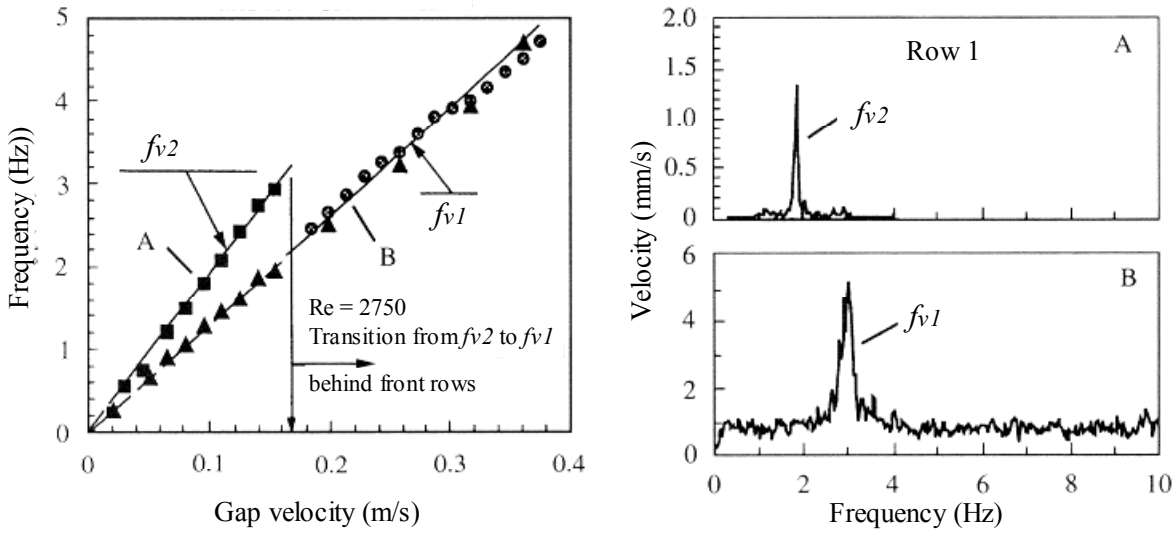

Figure 6.9. Frequency components of flow periodicity observed behind rows 1 & 5 in a large spacing parallel triangle array (X_p = 3.41), and two hot film spectra measured behind row 1 at velocities corresponding to points A & B. ■, ●, behind row 1; ▲, behind row 5.

The results of the arrays with intermediate and small pitch ratios have shown that a high-frequency component often appears at relatively low Reynolds numbers and subside when the Reynolds number is increased over ~ 6000. The lowest Reynolds number attainable in the air tests of this large spacing array was 5400. Therefore, in order to find out whether the high-frequency component also exists in this large spacing array at low Reynolds numbers, additional tests of an array with similar geometry were carried out in a water channel. The Reynolds number range of these tests was $0 < Re < 6500$. The frequency components of the flow periodicities measured by a hot film behind rows 1 and 5 of this array are plotted against the gap velocity in Fig. (6.9). Two flow periodicity components are detected in this Reynolds number range, $S_1 = 0.22$ and $S_2 = 0.31$. The component S_1 corresponds exactly to that measured in air. As observed in Fig. (6.9), the high-frequency component occurs mainly behind the front rows and at low Reynolds number ($Re <$ 2750), whereas the low-frequency component exists behind the inner rows at all Reynolds numbers. The high-frequency component disappears altogether when the Reynolds number is increased over 2750 and thereafter the low-frequency component dominates the whole array. This agrees with the general features of vorticity shedding excitation that a high frequency component exists at front rows and a lower component at the rear rows.

6.4. Strouhal Number of Vorticity Shedding in Parallel Triangle Arrays

The Strouhal numbers of the flow periodicities (vortex shedding) in parallel triangle arrays are given in Fig. (6.10). Since the data obtained from resonance cases may not always represent those of the natural flow periodicities, they are not included in this figure.

The Strouhal number in this chart is based on the frequency of flow periodicity, f_v, and the tube diameter, d, and is given by the Eq. (1):

$$S = f_v\, d/V_g \tag{1}$$

where the gap velocity, V_g, is given as a function of the upstream velocity V_u:

$$V_g = V_u\, [(2\, X_p\ \cos 30) / (2\, X_p\ \cos 30\ - 1)] \tag{7}$$

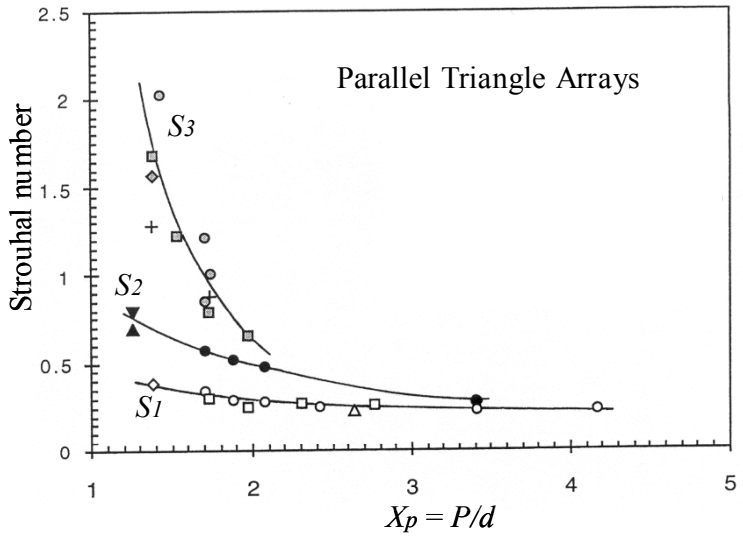

Figure 6.10. Strouhal number chart for vorticity shedding observed under non-resonant flow conditions in parallel triangle arrays.

The Strouhal number data are seen to collapse mainly around three different Strouhal number lines in Fig. (6.10). The line S_1 is associated with the lowest frequency observed. It corresponds to the frequency component f_{v1}, which dominates at deeper rows but is hardly discernible behind front rows at low Reynolds numbers. This component has been observed in the spacing range of $1.38 < X_p < 4.17$. S_1 has a value of 0.4 for $X_p = 1.38$ and it approaches a value of ≈ 0.2 in arrays with pitch ratios larger than 3.

The Strouhal number line S_2 in Fig. (6.10) corresponds to the frequency component f_{v2}. It is found to exist simultaneously with the S_1 component and appears to be bound to the front rows only. The Strouhal number designated with the line S_3 appears to be the characteristic of relatively small spacing arrays ($X_p < 2$). A wide scatter is observed in the data belonging to this group of Strouhal number. This Strouhal number is associated with the shear layer vortices developing in the flow lanes between the adjacent tube columns from the first row towards the rear rows. Therefore, the occurrence of this component is strongly Reynolds number dependent. While it is detected throughout the array at very low Reynolds numbers, it disappears totally at high Reynolds numbers.

6.5. Acoustic Response of Parallel Triangle Arrays

The acoustic response of normal triangle arrays is found to be somewhat similar to that of in-line arrays. In the majority of tested arrays, specially the small and intermediate spacing ratios, the onset of acoustic resonance did seem to be related to the vorticity shedding excitation which is observed before the onset of resonance. An example is shown in Fig. (6.11) for $X_p = 1.44$. The main frequency component of vortex shedding f_{v3} is shown by the solid line and the dashed lines represent the acoustic Strouhal numbers, S_a, which are based on the resonance frequency and the flow velocity at the onset of resonance.

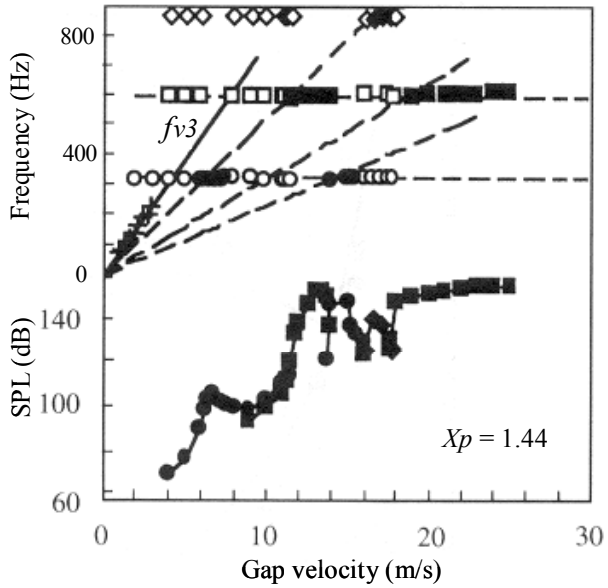

Figure 6.11. Acoustic response of a parallel triangle array with $X_p = 1.44$. +, vorticity shedding f_{v3}; ●, ■, , response of the first, second and third acoustic modes.

As can be seen, despite the presence of a well-defined flow periodicity in the array, f_{v3}, the first acoustic mode is excited not at the point of frequency coincidence but at a substantially higher velocity (about 60% higher than the coincidence velocity). As the flow velocity is increased further, the second and third acoustic modes are also excited. In fact, the resonances of these modes are relatively strong and have wide ranges of lock-in, although no periodic flow activities exist at these high velocities. The resonances seem to occur according to an *acoustic Strouhal number* relation

(the dashed lines), which could not be associated with the natural flow periodicity. Similar features were observed for other spacing ratios as reported by Ziada & Oengoeren (2000).

6.6. Acoustic Strouhal Number of Parallel Triangle Arrays

The acoustic responses of parallel triangle arrays indicated that for most of these arrays, the critical velocities for the onset of acoustic resonances cannot be predicted from the Strouhal numbers of the natural flow periodicities, which are detected at non-resonant conditions. This feature is different from that of normal triangle arrays, for which the acoustic Strouhal numbers have been found to approximate those of the natural flow periodicities (Oengoeren & Ziada, 1998). On the other hand, the acoustic behaviour of parallel triangle arrays is similar to that of in-line arrays. This similarity seems to stem from the fact that both array patterns allow the flow to proceed freely along the flow lanes between the tube columns.

In order to be able to predict the onset of acoustic resonance in parallel triangle arrays, an acoustic Strouhal number chart has been developed and is given in Fig. (6.12). The acoustic Strouhal number, S_a, is defined as:

$$S_a = f_a \; L \; / \; V_g \tag{8}$$

Where f_a is the acoustic resonance frequency and V_g is the critical gap velocity at the onset of acoustic resonance. As observed in Fig. (6.12), multiple acoustic Strouhal numbers exist in arrays with $X_p < 1.71$. Although some of these Strouhal numbers are associated with the resonance of all modes (from 1 to 3), some are related to only one mode. To avoid any misunderstanding, the acoustic modes excited by each Strouhal number are noted near each data point in Fig. (6.12). The curve displayed in this figure is the upper limit to the acoustic Strouhal numbers of the tested cases and should be treated as a design value to avoid acoustic resonances over the whole velocity range.

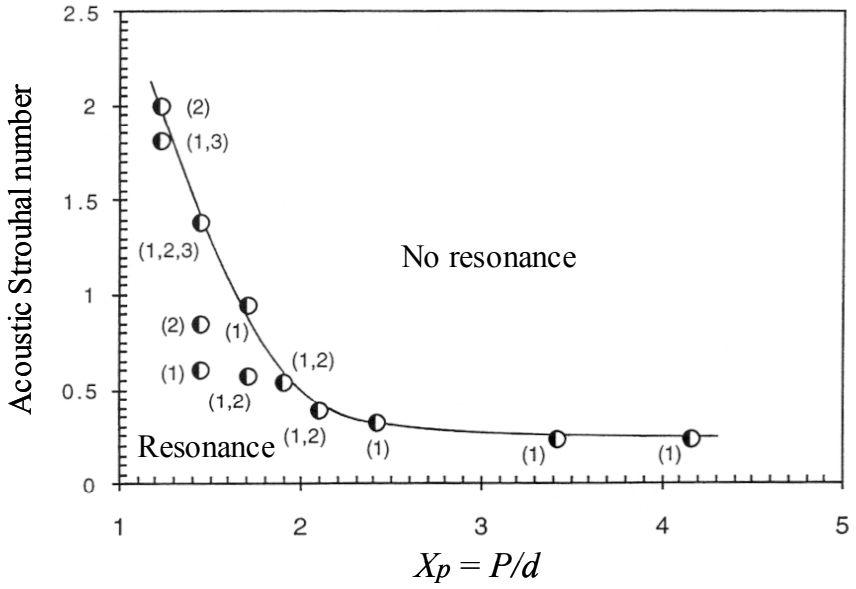

Figure 6.12. Acoustic Strouhal number chart for *parallel triangle arrays*. The acoustic modes excited are also provided near each data point.

The usage of the acoustic Strouhal number chart for design purposes can be demonstrated by considering the case with $X_p = 1.44$, which is illustrated in Fig. (6.11). As the flow velocity was increased, the lowest three acoustic modes were excited in a rather complex order. After the

resonance of modes 1 and 2, mode 1 was excited again. This was followed by mode-3 resonance, and finally mode 2. The acoustic Strouhal numbers of these resonances are indicated in Fig. (6.11). From a practical point view, estimation of the critical flow velocities corresponding to these Strouhal numbers is of little use. Instead, the designer should ensure that the Strouhal number based on the maximum flow velocity and any acoustic frequency is higher than the design limit given by Fig. (6.12).

The upper bound of the acoustic Strouhal numbers in Fig. (6.12) may appear similar to the envelope of the Strouhal numbers of the natural flow periodicities which are depicted in Fig. (6.10). However, this is true only for large spacing ratios, $X_p > 2.3$, which is to be expected, since alternating vortex shedding becomes dominant. For smaller spacing ratios, S_3 can be up to 54% higher than the acoustic Strouhal number.

6.7. Summary of Results for Parallel Triangle Arrays

Natural flow periodicities in parallel triangle arrays occur at three different Strouhal numbers, S_1, S_2 and S_3. The highest Strouhal number, S_3, is associated with the instability of the shear layer which develops on the sides of the flow lanes between the tube columns. This type of flow periodicity exists only in arrays with pitch ratios smaller than 2. Moreover, they are sustained only at relatively low Reynolds numbers. The Strouhal number S_2 is associated with alternating vortex shedding behind the first two rows. It subsides when the Reynolds number is sufficiently increased and is replaced by the periodicity S_1. The Strouhal number S_1 is associated with alternating, large-scale vortex shedding in the wakes of the inner tubes. It is observed in arrays with $X_p > 1.4$ in this study and in the literature. At high Reynolds numbers, this periodicity dominates in the whole array, i.e., also at the front rows. A Strouhal number chart is provided for the natural flow periodicities in parallel triangle arrays.

For the arrays with $X_p \leq 2.42$, the onset of acoustic resonances could not be related to the natural flow periodicities which are observed before the onset of resonances. This contrasts with the acoustic response of normal triangle arrays for which the resonance has been found to be excited by the natural flow periodicities. A chart for the acoustic Strouhal number for parallel triangle arrays is provided. The excitation mechanism of acoustic resonance in parallel triangle arrays seems to be similar to that of in-line arrays. The reasons for this similarity must lie in the fact that both arrays allow the flow to proceed along the free-flow lanes between the tube columns, which result in a similar interaction mechanism between the flow instability and the sound waves.

7. Dynamic Fluid Forces on the Tubes

The dynamic fluid forces acting on the tubes of any bundle are caused by two mechanisms; vorticity (or vortex) shedding and flow turbulence. The first is controlled by the nature of vorticity shedding, which has been already discussed for all tube patterns. For example, staggered arrays generally have a high Strouhal number at the front rows and a low one at the inner rows. In contrast, in-line arrays have a single vorticity component. The turbulence spectra at the inner rows for all arrays are expected to have some common features because, deep inside the bundle, the tubes are the main turbulence generators. Thus, the main parameters which control the maximum level of the fluid forces are the pitch ratio and the Reynolds number. In this section, the fluid forces acting on the tubes are addressed and the highest levels of these forces are deduced. This requires force measurements at many rows to make sure that the maximum values are captured. Only selected results of dynamic fluid forces are given here and the reader is referred to Oengoeren & Ziada (1992b, 1998) for further details.

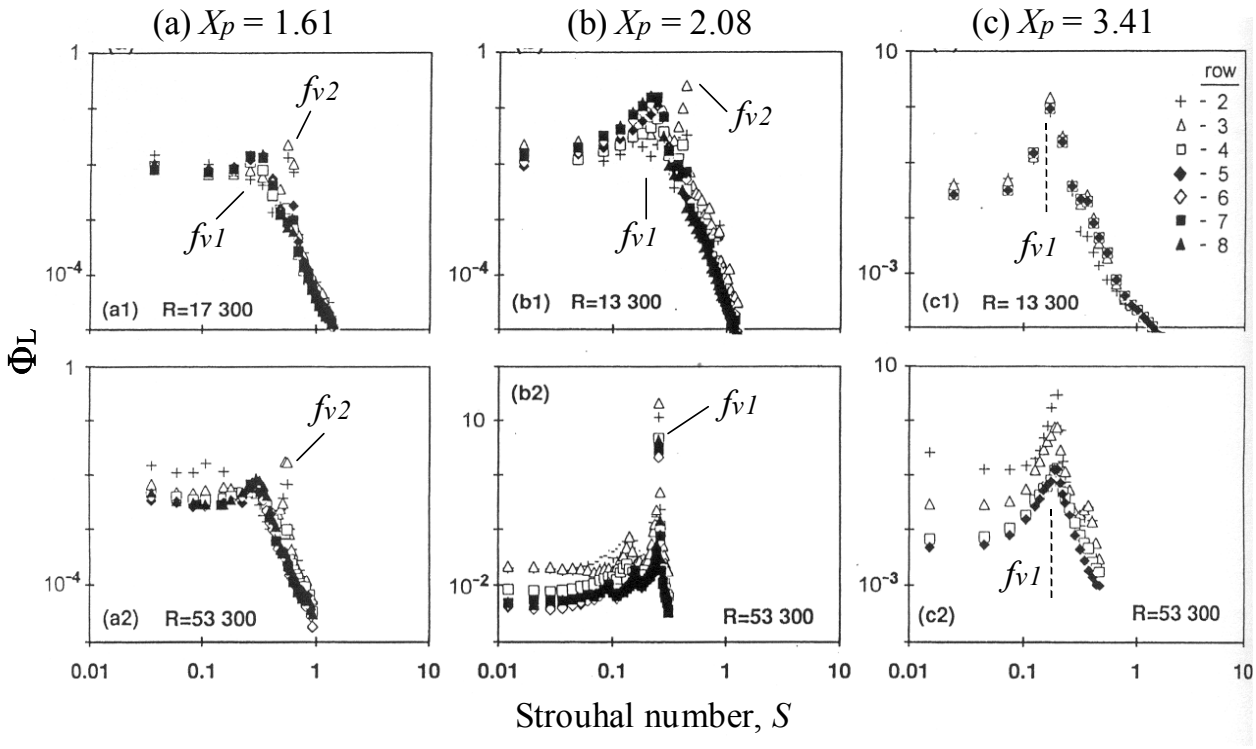

Figure 7.1. Normalized power spectral densities of dynamic lift forces (Φ_L) measured on rows 2 to 8 in *normal triangle arrays* with (a) X_p= 1.61, (b) X_p= 2.08 and (c) X_p= 3.41 for two Reynolds numbers.

7.1. Spectral Densities of Dynamic Forces

Oengoeren & Ziada performed extensive measurements to obtain the power spectral densities (PSD) of the dynamic lift and drag forces for in-line and staggered arrays with different spacing ratios. For each array, forces on the first 8 rows at three different Reynolds numbers were made to insure capturing the maximum level of fluid forces which is a function of tube location and Reynolds number. As an example, the results of normal triangle arrays are discussed here.

The *normalized* PSD of the lift force, Φ_L, for two Reynolds numbers are plotted in Fig. (7.1) for the three arrays discussed in Section 3. The normalized PSD is defined by:

$$\Phi_L = \frac{F_L}{[(1/2)\,\rho\, V_g^2\, \ell\, d]^2} \left(\frac{V_g}{d}\right) \tag{9}$$

where F_L is the power spectral density of the dynamic lift force, ρ is the fluid density and ℓ is the tube length. It is seen that the normalization of PSD reduces the data of each array to a characteristic distribution.

For the intermediate spacing array, X_p = 2.08, Φ_L at the lower Reynolds number value, Fig. (7.1.b1), has two peaks around the Strouhal numbers of 0.26 and 0.4 which correspond to the components f_{v1} and f_{v2} of vortex shedding. The higher frequency peak f_{v2} appears only at rows 2 and 3, whereas the lower frequency peak f_{v1} is dominant at the inner rows. At the higher Reynolds number value, Fig. (7.1.b2), the f_{v1} peak becomes stronger, narrow banded and dominant, whereas the f_{v2} component subsides. These features of the force are in accordance with the characteristics of the developing flow as discussed in Section (3).

As the tube spacing is reduced to X_p = 1.61, the f_{v1} component becomes much weaker as observed in Fig. (7.1.a). The f_{v2} component remains, however only at the front rows. The PSD data of the rear rows collapse to a single distribution having a form similar to that generated by a turbulence excitation. The effect of neither the Reynolds number nor the row depth is significant on the magnitude of the PSD.

In contrast with the small spacing case, as the spacing is increased to X_p = 3.41, the f_{v2} peak disappears from the PSD distributions for the Reynolds numbers considered in Fig. (7.1.c). Here, the peak appearing around S = 0.2 corresponds to the component f_{v1}. In this array, the row depth does not have any effect on the PSD at the low Reynolds number value, Re = 13300. However, at the high Reynolds number value, Re = 53300, an order of magnitude difference is observed between the PSD of the front and the rear rows.

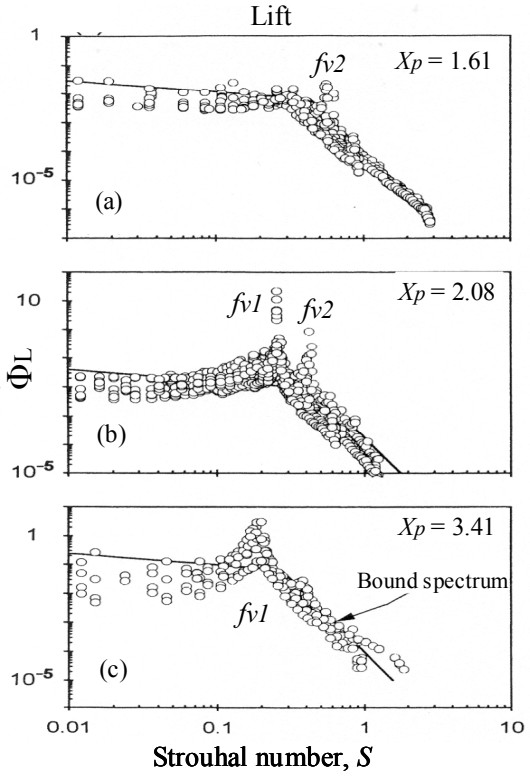

Figure 7.2. Normalized power spectral densities of dynamic lift force in *normal triangle arrays* with three different spacing ratios. The results cover a Reynolds number range of 13300< Re < 53300 and tubes in rows 2 to 8.

After it was introduced by Mulcahy (1984), the so-called bound spectrum concept has emerged as an adequate tool for the prediction of the turbulent forces exerted on the tubes of heat exchanger arrays (Taylor et al. 1988, Axisa et al. 1990 and Oengoeren and Ziada 1992b). In order to obtain these bound spectra, first the PSD of the dynamic forces for all measured rows (2 to 8) and for all Reynolds numbers covered in the experiment were compiled on one graph as shown in Fig. (7.2). Then, a spectral bound which envelopes all the data except the vorticity shedding peaks was determined for each spacing ratio. The bound corresponding to each case is drawn as a solid line in Fig. (7.2). The peaks of vorticity shedding excitation are excluded from the bound spectra because such an excitation is strongly dependent on the spacing ratio and Reynolds number. A vortex shedding peak which exists in large spacing arrays does not necessarily exist in small spacing arrays of similar pattern. Furthermore, the Strouhal numbers of such peaks are also spacing ratio dependent. Therefore, the inclusion of these peaks in the bound spectra makes the use of such spectra very impractical and would result in *very conservative* designs of closely packed arrays.

The bound spectra of the three spacing ratios are reproduced in Fig. (7.3) and their equations are listed in the table attached to the figure. The highest level of dynamic forces in the lower frequency range (S < 0.4) is measured in the large spacing case. As the spacing ratio is reduced to the intermediate and the small spacing cases, the level of the dynamic forces decreases. However, the difference in the levels of bound spectra of these two cases is negligibly small. Furthermore, the dynamic forces of all geometries seem to approach to the same bound in the upper frequency range (S > 0.4). As expected, the drag forces were found to be substantially smaller than the left forces and are therefore not given here for the sake of brevity. Similar information for in-line tube bundles can be found in Oengoeren & Ziada (1992b).

PITCH RATIO	BOUND SPECTRUM	STROUHAL NO. RANGE
$X_p = 1.61$	$\phi_L = 4.75 \times 10^{-3}\ S^{-0.4}$ $= 1.02 \times 10^{-4}\ S^{-5}$	$S < 0.43$ $S > 0.43$
$X_p = 2.08$	$\phi_L = 6.34 \times 10^{-3}\ S^{-0.4}$ $= 1.80 \times 10^{-4}\ S^{-5}$	$S > 0.46$ $S > 0.46$
$X_p = 3.41$	$\phi_L = 3.87 \times 10^{-2}\ S^{-0.4}$ $= 1.00 \times 10^{-4}\ S^{-5}$	$S > 0.27$ $S > 0.27$

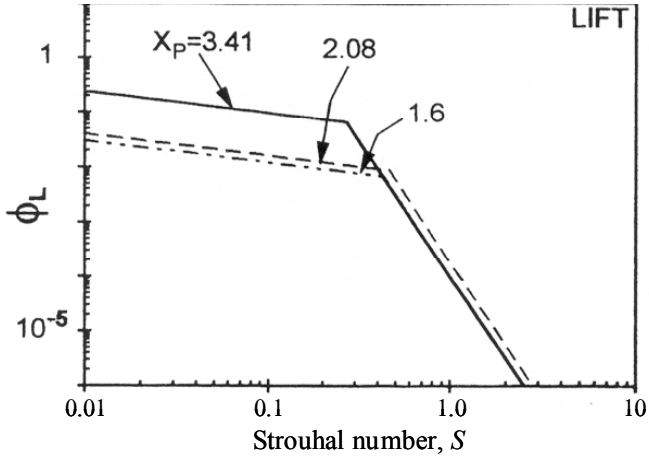

Figure 7.3. Bound spectra of dynamic lift force for three *normal triangle arrays* with small, intermediate and large spacing ratios. The table shows the equations of the bound spectra.

7.2. Dynamic Lift and Drag Coefficients

The overall effect of the dynamic forces exerted on the tubes, including the effect of vortex shedding excitation, can be represented by classical force coefficients. In the following, the root mean square (rms) values of the dynamic lift and the drag coefficients are presented. The force coefficient, C, is defined as:

$$C = (\int \Phi \, dS)^{1/2} \qquad (10)$$

where Φ is the normalized PSD and S is the Strouhal number. The upper limit of the integration corresponds to the upper frequency limit of the force measurements, which was 800 Hz.

The lift and the drag coefficients calculated from the PSD distributions are plotted in Fig. (7.4) for three normal triangle arrays with different spacing ratios. A strong dependence of the force coefficients on the spacing ratio is observed in this figure such that at a given row the level of the lift and the drag coefficients increases gradually with increasing spacing ratio. In all three geometries, the maximum level is reached around the second or the third rows. The force

coefficients belonging to the inner rows are lower to varying degrees, depending on the spacing ratio.

The maximum values of the lift coefficient, taken from Fig. (7.4), are compiled as functions of the Reynolds number and the spacing ratio in Fig. (7.5) to provide a design chart for tube vibration calculations. As observed in this figure, the Reynolds number has insignificant effect on the lift coefficient for the arrays with spacing ratios less than 1.6. For spacing ratios larger than 1.6, the lift coefficient becomes dependent on the Reynolds number which has the most pronounced effect in the intermediate spacing case.

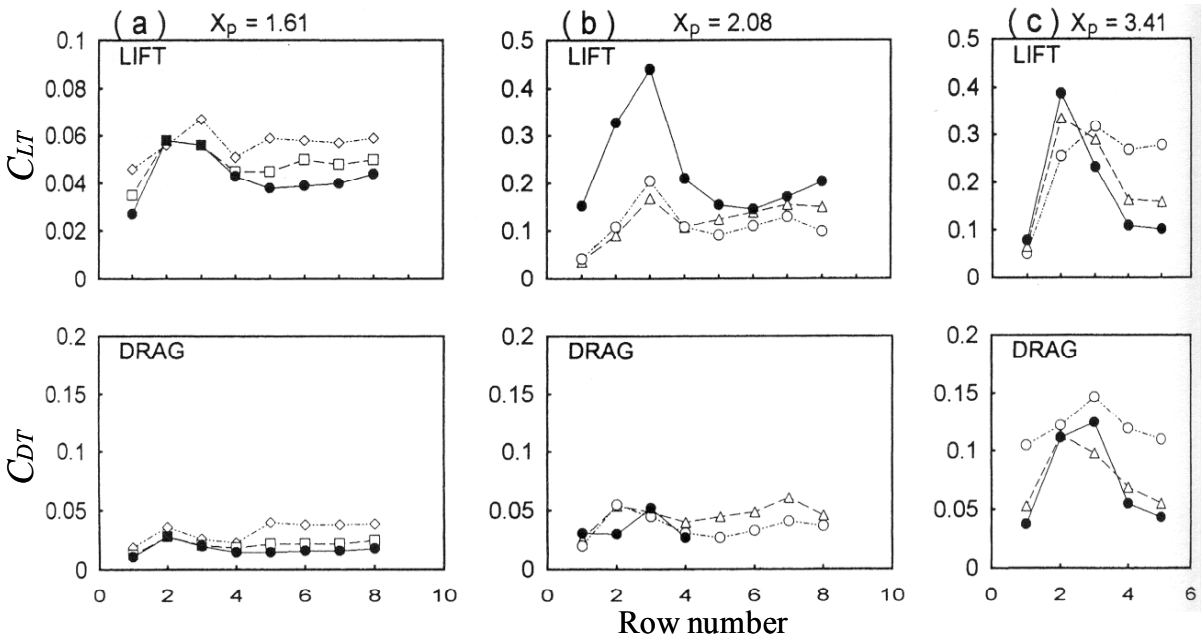

Fig. 7.4: Total dynamic lift and drag coefficients (C_{LT} & C_{DT}) as functions of row depth in (a) small, (b) intermediate and (c) large spacing *normal triangle arrays*. ○, Re = 13300; ◊, 17300; Δ, 26600; □, 33300; ●, 53300.

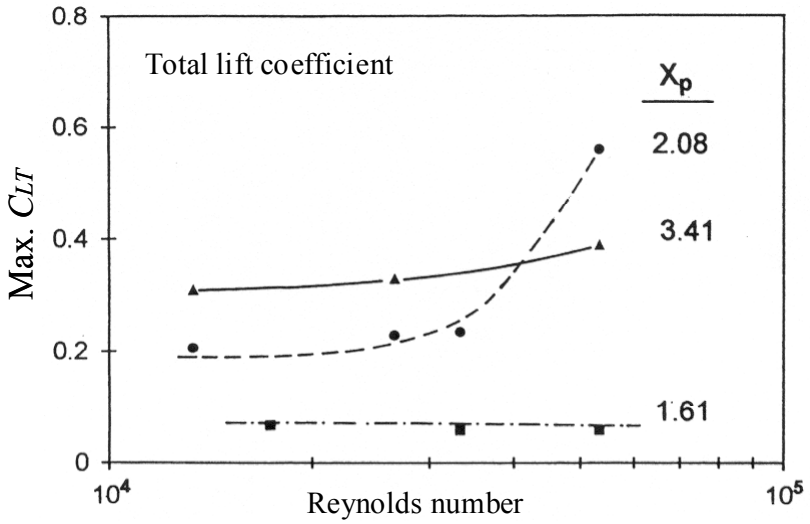

Figure 7.5. Distribution of maximum dynamic lift coefficients (Max C_{LT}) as functions of Reynolds number for three *normal triangle arrays* with the spacing ratios X_p = 1.61, 2.08 and 3.41.

8. References

Axisa, F., Antunes, J. & Villard, B., 1990, “Random Excitation of heat exchanger tubes by cross-flows”, Journal of Fluids and Structures 4, pp. 321-341.

Bajaj, A. K. & Garg, V. K., 1977, “Linear stability of jet flows”, Journal of Applied Mechanics 44, pp. 378-384.

Blevins, R. D. & Bressler, M. M., 1987a, “Acoustic resonance in heat exchanger tube bundles-Part I: physical nature of the problem”, Flow Induced Vibration 1987, PVP-Vol.122 (eds. M. K. Au-Yang & S. S. Chen), pp. 19-26. New York: ASME.

Blevins, R. D. & Bressler, M. M., 1987b, “Acoustic resonance in heat exchanger tube bundles-Part II: prediction and suppression of resonance”, Flow Induced Vibration 1987, PVP-Vol.122 (eds. M. K. Au-Yang & S. S. Chen), pp. 27-34. New York: ASME.

Blevins, R. D. & Bressler, M. M., 1992, “Experiments on acoustic resonance in heat exchanger tube bundles”, Proceedings of ASME 1nternational.Symposiumon on Flow Induced Vibrations and Noise, Vol. 4: Acoustical effects in FIV (eds. M. P. Païdoussis & J. B. Sandifer), pp. 59-79, New York: ASME.

Chen, Y. N., 1968, “Flow-induced vibration and noise in tube-banks of heat exchangers due to von Karman streets”, ASME Journal of Engineering for Industry 90, pp. 134-146.

Eisinger, F. L., Sullivan, R. E. & Francis, J. T., 1992, “A review of acoustic vibration criteria compared to in-service experience with steam generator in-line tube banks”, Proceedings of ASME International Symposium on Flow Induced Vibrations and Noise, Vol. 4: Acoustical Effects in FIV (eds. M. P. Païdoussis & J. B. Sandifer), pp. 81-95, New York. ASME.

Fitzpatrick, J. A., 1986, “A design guide proposal for avoidance of acoustic resonances in in-Iine heat exchangers”, ASME Journal of Vibrations, Acoustics, Stress and Reliability in Design 108, pp. 296-300.

Freymuth, P., 1966, “On transition in a separated Laminar boundary layer”, Journal of Fluid Mechanics 25, pp. 683- 704.

Howe, M.S., 1975, “Contribution to the theory of aerodynamic sound, with application to excess jet noise and the theory of the flute”, Journal of Fluid mechanics 71, pp. 625-673.

Howe, M.S., 1980, “The dissipation of sound at an edge”, Journal of Sound and Vibration 70, pp. 407-411.

Michalke, A., 1965, “On spatially growing disturbances in an inviscid shear layer”, Journal of Fluid Mechanics 23, pp. 521-544.

Miksad, R. W., 1972, “Experiments on the nonlinear stages of free-shear transition”, Journal of Fluid Mechanics 56, pp. 695-719.

Miksad, R. W., 1973, “Experiments on non-linear interaction of a free shear layer”, Journal of Fluid Mechanics 59, pp. 1-21.

Mulchahy, T. M., 1984, “Fluid forces on a rigid cylinder in turbulent cross-flow”, Proceedings of ASME International Symposium on Flow-Induced Vibration, Vol. 2: Excitation and Vibration of Bluff Bodies in Cross Flow (eds. M. P. Païdoussis, O. M. Griffin & M. Sevik), pp. 15-28, New York: ASME.

Oengoeren, A. & Ziada, S., 1992a, "Vorticity shedding and acoustic resonance in an in-line tube bundle - Part II: Acoustic resonance”, Journal of Fluids and Structures 6, pp. 293-309.

Oengoeren, A. & Ziada, S., 1992b, "Unsteady fluid forces acting on a square tube array in air cross-flow", Proceedings of the 3rd International Symposium on Flow-Induced Vibration and Noise, ASME WAM, Anaheim, Vol. 1, pp. 55-74.

Oengoeren, A. & Ziada, S., 1998, "A comprehensive study of vortex shedding, acoustic resonance and turbulent buffeting in normal triangular tube bundles", Journal of Fluids and Structures 12, pp. 717-758.

Owen, R. R., 1965, “Buffeting excitation of boiler tube vibration”, Journal of Mechanical Engineering Science 7, pp. 431-439.

Païdoussis, M. P., 1982, “A review of flow-induced vibrations in reactors and reactor components”, Nuclear Engineering and Design 74, pp. 31-60.
Rockwell, D. & Naudascher, E., 1979, “Self-sustained oscillations of impinging free shear layers”, Annual Review of Fluid mechanics 11, pp. 67-94.
Sato, H., 1960, “The instability and transition of a two-dimensionsl jet”, Journal of Fluid Mechanics 7, pp. 53-80.
Taylor, C. E., Pettigrew, M. J., Axisa, F. & Villard, B., 1988, “Experimental determination of single and two-phase cross flow-induced forces on tube rows”, ASME Journal of Pressure Vessel Technology 110, pp. 22-28.
Weaver, D. S., 1993, “Vortex shedding and acoustic resonance in heat exchanger tube arrays”, Technology for the '90s (ed M. K. Au-Yang), pp. 776-810. New York: ASME.
Weaver, D. S., Lian, H. Y. & Huang, X. Y., 1993, “Vortex shedding in rotated square arrays”, Journal of Fluids and Structures 7, pp. 107-121.
Ziada, S. & Oengoeren, A., 1992, "Vorticity shedding and acoustic resonance in an in-line tube bundle - Part I: Vorticity shedding", Journal of Fluids and Structures 6, pp. 271-292.
Ziada, S. & Oengoeren, A., 1993, "Flow structures in an in-line tube bundle with large tube spacings", Journal of Fluids and Structures 7, pp. 661-687.
Ziada, S. & Oengoeren, A., 2000, "Flow periodicity and acoustic resonance in parallel triangle tube bundles", Journal of Fluids and Structures 14, pp. 197-219.
Ziada, S., Oengoeren, A. & Buehlmann, E.T., 1989a, "On acoustical resonances in tube arrays - Part I: Experiments", Journal of Fluids and Structures 3, pp. 293-314.
Ziada, S., Oengoeren, A. & Buehlmann, E.T., 1989b, "On acoustical resonances in tube arrays - Part II: Damping criteria", Journal of Fluids and Structures 3, pp. 315-324.
Ziada, S. & Rockwell, D., 1982, "Generation of higher harmonics in a self-oscillating mixing layer-wedge system", AIAA Journal 20, pp. 196-202.

9. Copyright Notice